Laboratory hydration of condensed magnesiosilica smokes with implications for hydrated silicates in IDPs and comets

Frans J. M. RIETMEIJER,[1*] Joseph A. NUTH, III,[2] and Robert N. NELSON[3]

[1]Department of Earth and Planetary Sciences, University of New Mexico, Albuquerque, New Mexico 87131–1116, USA
[2]Laboratory for Extraterrestrial Physics, Code 691, NASA Goddard Space Flight Center, Greenbelt, Maryland 20771, USA
[3]Code 691, NASA Goddard Space Flight Center, Greenbelt, Maryland 20771, USA
[*]Corresponding author. E-mail: fransjmr@unm.edu

Abstract–Samples of silica-rich and MgO-rich condensed, amorphous magnesiosilica smokes were hydrated to monitor systematic mineralogical and chemical changes as a function of time and temperature controlled by their unique metastable eutectic compositions, their porous texture, and the ultrafine, nanometer grain size of all entities. At water supersaturated conditions, proto-phyllosilicates formed by spinodal-type homogeneous nucleation. Their formation and subsequent growth was entirely determined by the availability of water via pore spaces inherited from the original smokes and the textural continuity of magnesiosilica material with a mostly smectite-dehydroxylate composition. The results may have implications for the hydration of proto-CI material, the presence of rare periclase and brucite in primitive solar system bodies, and the pervasiveness of hydrated amorphous magnesiosilica dust and saponite proto-phyllosilicates in icy-protoplanets, such as comet nuclei.

INTRODUCTION

It is often stated that anhydrous, aggregate interplanetary dust particles (IDPs) are cometary dust and that hydrated IDPs are debris from hydrated asteroids (Brownlee 1985; Bradley 1988; Zolensky and Barrett 1994). This notion presumes that aqueous activity cannot occur in comet nuclei. It also presumes that layer silicates occur only in CI and CM chondrites representing aqueous environments at temperatures between 293 K and 400 K that were conducive to pervasive layer silicate formation (Zolensky and McSween 1988; Bunch and Chang 1980). Layer silicates in the Alais CI chondrite are fine-grained, <50 nm × <100 nm, montmorillonite-type clay minerals with an anastomosing texture and poorly defined crystallinity plus serpentine compositions, <100 nm × <600 nm (Mackinnon and Kaser 1988). Phyllosilicates are secondary minerals because they formed via aqueous alteration of anhydrous precursor materials. Under terrestrial or geological conditions, that process requires time, although how much time will depend, among other factors, on the grain size of the precursor minerals (Wegner and Ernst 1983; Fegley 1988). At the micrometer-scale and smaller, which is typical for extraterrestrial materials, diffusion may not be a rate-limiting process because, for increasingly smaller grains, surface diffusion, rather than volume diffusion, will control the

hydration process. The amorphous or crystalline nature of the anhydrous precursor is another variable in this process. For example, it was previously accepted that the layer silicates in meteorites had formed at low temperatures in the solar nebula when water reacted with stoichiometric silicate mineral dust that had formed by fractional equilibrium condensation in a cooling solar nebula of chondritic composition (Grossman and Larimer 1974). However, hydration of condensed stoichiometric olivine and pyroxene crystals to serpentine and smectite, respectively, will not be efficient under nebula conditions because of low water-vapor pressure. It requires breaking bonds of the crystal lattice and a delicate balance between the water-vapor temperature and the precursor grain size (Fegley 1988). These requirements were obviously met in the carbonaceous chondrite parent bodies wherein water was widely available. The situation was different in the unequilibrated ordinary chondrite parent bodies, although proto-phyllosilicates, including saponite, are commonly found in the amorphous matrix of these meteorites where conditions were adequate to support hydration reactions (Alexander et al. 1989; Brearley 1993; Zolensky et al. 1993). Similarly proto-phyllosilicates form at very short time scales in volcanic glasses (Tazaki et al. 1989; Rietmeijer 1992). Proto-phyllosilicate formation is undoubtedly facilitated by an amorphous state of the precursor because there is no need to break crystal bonds.

Since ultrafine-grained amorphous solids will be highly susceptible to hydration, it is germane to address the possibility of layer silicate formation in the extreme environments of icy, outer belt asteroids and in Oort cloud and Kuiper Belt comet nuclei. Intuitively, the infrared (IR) class P- and D-type bodies, which include a majority of the near-Earth asteroids (Bell et al. 1989; Hartmann et al. 1987), would not appear to be conducive to containing liquid water. Its presence in these icy protoplanets has yet to be proven, though it is known that a layer of liquid water forms on dust grains embedded in ice at temperatures below the melting point (Rietmeijer 1985). It was theorized that a thin (~0.6 to 8 nm) interfacial water layer, first found in terrestrial permafrost, could support hydrocryogenic alteration near the surface of icy protoplanets near perihelion (Rietmeijer 1998). It is interesting to note that layer silicates were found in the Tagish Lake meteorite, which has D-type IR spectral features (Brown et al. 2000). While it will be an unlikely scenario to form layer silicates in outer-belt asteroids, tiny pools of water might exist underneath the black mantle of active short-period comets at perihelion (Rietmeijer 2002a). Layer silicates could be up to 8% of the dust in comet Halley (Jessberger et al. 1988) and could include Na-bearing smectite (Rietmeijer et al. 1989).

Another reason that layer silicates might be common in the extreme environment of icy protoplanets is because of a unique chemical property of the accreted dust. While upholding the axiom that all solids in circumstellar dust environments were initially formed by vapor phase condensation, recent experiments showed that non-equilibrium condensation yields metastable, ferrosilica, and magnesiosilica dusts with serpentine- and smectite-dehydroxylate compositions, that is, solids with the M/Si (M = Mg, Fe, Al) ratios of these layer silicates but wherein the amount of stoichiometric layer silicate $(OH)^-$ is replaced by the appropriate amount of O^{2-} (MacKenzie and Meinhold 1994; Nuth et al. 2002; Rietmeijer et al. 2000). The results of these condensation and thermal annealing experiments predicted the compositions of the Mg-rich ferromagnesiosilica dust in the matrix of chondritic aggregate IDPs (Rietmeijer et al. 1999a) and in comet Halley (Rietmeijer 1998, 2002a). These results also constrained the minerals in active olivine-rich comets (Hallenbeck et al. 1998; Fabian et al. 2000; Rietmeijer et al. 2002a) and the forsterite to silica ratios in dust around young stellar objects (Bouwman et al. 2001).

Here, we report the petrological development, including proto-phyllosilicate and layer silicate formation, during hydration experiments of condensed amorphous magnesiosilica smokes (Nuth et al. 1986). Nelson et al. (1987) determined the hydration rates of these samples based on the IR spectral evolution as a function of time and temperature. We also report on proto-phyllosilicates and layer silicates that formed during hydration of MgO-rich magnesiosilica smoke at high temperatures (423 K; 573 K)

for reaction times of up to 72 hr. The samples were selected to explore the compositional and textural control on hydration and kinetically controlled formation of proto-phyllosilicates and layer silicates in condensed materials that may serve as analogues for dust modification in active comet nuclei.

EXPERIMENTAL

Condensation of Starting Materials

Magnesiosilica smokes were prepared using two different methods. The first method, based on vaporization and recondensation, employed an apparatus wherein silicon monoxide and magnesium metal in separate alumina crucibles that were placed closely together were heated in a H_2 gas at total pressures from 20 to 50 torr (Nuth and Donn 1983). The measured temperature of the evaporators could be controlled to within a few degrees over a range of 900 K to 1550 K. The temperature profile of the furnace that controlled the temperature of the ambient H_2 gas could be regulated to within a few degrees over the range of 700 K to 1075 K. The furnace temperature simultaneously controlled both the temperature of the ambient gas and the magnesium crucible temperature and, thus, also controlled the partial pressure of magnesium in the nucleation region (Nuth and Donn 1983). The system was fitted to monitor the amount of Mg vapor present in the furnace and the onset of nucleation. The condensed smoke was collected near the top of the furnace for subsequent characterization (Nelson et al. 1987).

The second method used the Condensation Flow Apparatus wherein magnesiosilica smoke is produced by condensation of Mg-SiO-H_2-O_2 vapor (Nelson et al. 1989; Nuth et al. 1998). In this apparatus, there is no standard set of flow, temperature, or pressure settings, but the following conditions are all at least somewhat typical of an average experiment. The total pressure in the system is ~100 torr. At the flame front in the furnace, temperature excursions as high as ~1,575 K may occur, though downstream in the steady-state furnace, the temperature is ~775 K. The hydrogen flow rate is ~1000 sccm (standard cubic centimeters per minute). Magnesium metal is placed into a graphite boat inside the apparatus. At the nominal 775 K temperature, magnesium metal has a vapor pressure of ~5 torr. The oxygen flow rate always equals or exceeds that of the introduced silane (SiH_4) but is usually within a factor of two of the silane setting. The silane flow rate is typically ~100 sccm (Hallenbeck et al. 1998). The hydrogen to oxygen ratio is always >5, as silane also contributes some amount of hydrogen. The typical oxygen flow is sufficient to just balance the hydrogen contributed from the silane flow to produce water and Si^0 without affecting the bulk flow of hydrogen. The oxygen fugacity is a dynamic quantity that is dependent on reaction rates rather than a thermodynamic quantity. The actual

oxygen fugacity during condensation is conducive to formation of silicon oxides such as SiO and Si_2O_3, which is the dominant condensed silica species in the vapor, some SiO_2 instead of Si^0, and MgO rather than Mg metal, although some magnesium metal is observed (Nuth and Donn 1983). The chamber wherein $Mg-SiO-H_2-O_2$ vapor condensation occurred may have contained some undetermined, but likely small, amount of water due to direct reaction of H_2 and O_2 (Rietmeijer and Nuth 2001).

Hydration Experiments

The samples prepared in a single batch by each method were stored at room temperature inside a desiccator in a helium atmosphere before the hydration experiments. The hydration experiments followed the procedure that was used by Nelson et al. (1987). That is, ~3 mg of sample was rinsed at room temperature in 2 ml of de-ionized water and placed in closed tubes. This procedure caused a slight effervescence when (probably) metallic magnesium in the condensed samples reacted with water, producing H_2. Typically 6 to 8 closed tubes were placed in an aluminum block that was preheated to the desired temperature before this block with the tubes was put inside the oven for hydration at a pre-determined time and temperature. The massive aluminum block insured rapid heating of the samples to the desired temperature. After an experiment was completed, the tubes were brought to room temperature, frozen at ~200 K using dry ice to quickly halt the hydration process and then freeze-dried for at least 6 hr in a vacuum to remove residual, unbound water. A standard KBr pellet was prepared for IR analysis.

Analytical and Transmission Electron Microscope (ATEM) Analyses

Serial ultrathin (~90 nm), electron-transparent sections were prepared from a small portion of each sample. Sections were placed on a holey carbon thin-film supported by a standard 200 mesh Cu grid for study in a JEOL 2000FX ATEM operated at an accelerating voltage of 200 keV. The TEM was equipped with a Tracor-Northern TN-5500 energy-dispersive spectrometer (EDS) for in situ quantitative chemical analysis with a relative error <10% using a probe size of ~10–20 nm in diameter, which, in most cases, is similar to the grain size or smaller. Artifacts in grain composition could arise from overlapping grains smaller than the section thickness. Before analysis, each grain was viewed using a "through-focus" technique to check for additional grains present along the electron beam path; the location for each EDS analysis was recorded on TEM micrographs. Grain overlap during analyses of grains in the starting material was not a problem in this study. We report only high fidelity grain analyses. Imaging in the TEM viewing mode is at a 0.2-nm

spatial resolution. Grain sizes were measured directly from calibrated TEM images with a 10% relative error. The structural properties, e.g., amorphous or crystalline, were obtained by selected area electron diffraction (SAED) analyses. Mineral identifications were based on the reported interplanar (d-) values based on calibrated polycrystalline ring patterns with a 10% relative error and the lattice fringe spacing, measured with a 10% relative error, in combination with chemical composition. For reduction of the lattice fringe data, it is critical to note that crystallites with distinctly different lattice fringe spacings co-occur in the same TEM image. The small differences are real and will be considered when comparing fringe spacing data among hydrated samples. We noted that the proto-phyllosilicates in these samples have sufficient thermal stability to maintain the integrity of the basal plane spacing. It seems possible that the surface-free energy of the nm-sized crystallites contributes to their stability in the incident electron beam.

The statistical analyses presented in this paper include a test of the normal distribution using the ratio of data range and the standard deviation (1σ) as a function of population size at a chosen 95% level of confidence. The Student's t-test was used, at a 10% significance level, to explore the whether the population means for two distributions could be from the same population or whether they have to be from two different populations.

<div align="center">

OBSERVATIONS

</div>

A Silica-Rich Smoke: Starting Material and Hydrated Samples

This silica-rich starting material produced by vaporization and re-condensation has an estimated bulk composition of <12 wt% MgO (Rietmeijer 1995). This value is based on the measured modal bulk composition of the smoke fraction (see below) plus the compact clusters and irregular patches of pure silica condensates. The samples selected included the starting material and those that were hydrated at: 1) 357 K for 48 hr, 72 hr (two different samples), and 96 hr; 2) 368 K for 9.1 hr; and 3) 378 K for 3 and 7.5 hr. For details and IR data, see Nelson et al. (1987).

Texture

The condensed fluffy (porous) material is an intimate mixture of magnesiosilica and pure silica smokes that both show the typical necklace texture (Fig. 1). The latter is more abundant than magnesiosilica smoke. The relative proportions of silica and magnesiosilica smoke domains are locally highly variable. The spherical grains in the silica smoke range from 25 to 90 nm in diameter ($\mu = 57$ nm; $1\sigma = 14.6$). The spherical "MgSiO" grains range from 7 to 36 nm in diameter (mean [μ] = 19.4 nm; one standard deviation [1σ] = 7.3 nm). Both grain populations are Gaussian distributions.
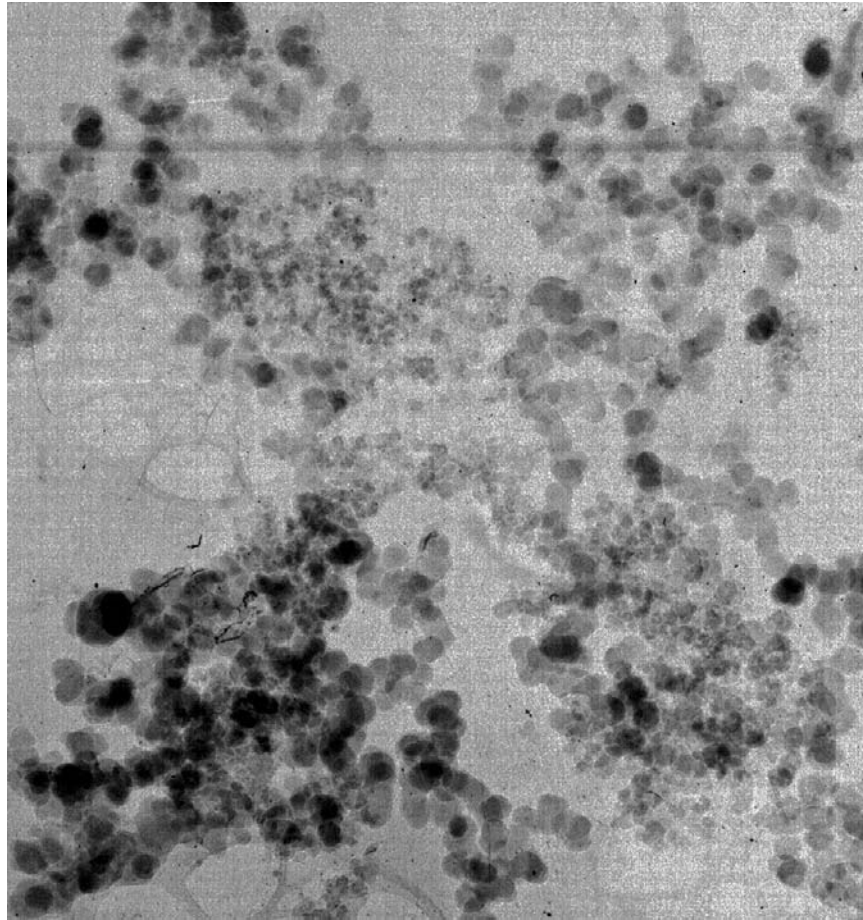
Fig. 1. Low magnification transmission electron microscope image showing the fluffy (porous) necklace texture of the condensed Si-rich magnesiosilica smoke used as the starting material for the hydration experiments. The sample is an intimate mixture of domains of pure, typically fine-grained MgSiO-smoke (center) and coarser-grained, pure silica smokes (dark material). In the lower right-hand corner, both smokes are in close contact. The field of view is 1.7 microns square. The gray background is the embedding epoxy used for ultramicrotome sectioning and the holey carbon support thin-film.

Patches of fluffy silica smoke show a gradual transition to massive clusters (up to 100 nm) of still visible condensed grains and to irregular patches with no traces of individual grains. Only small pores are the reminders of a porous smoke. These patches can be merged into large (~200 nm) areas with abundant spherical and irregular pore spaces. To a much lesser extent, there are similar but more localized transitions of the fluffy magnesiosilica smoke to dense spheres 40 to 165 nm in diameter that often show ~1 to 3 nm-sized tridymite domains.

In hydrated samples, the silica smoke with the original grain size range is still present after 96 hr at 357 K. However, the condensed silica smoke domains intermixed in the magnesiosilica smoke had almost disappeared after 48 hr. There are now abundant, mostly isolated, pure silica spheres (70–120 nm in diameter) generally surrounding domains of magnesiosilica smoke (Fig. 2). The sphere interior shows a radial pattern of shrinkage cracks. The condensed magnesiosilica grains in necklaces are pulled together into irregular grains and rings (cages) with outlines that initially delineate the fused grains but which slowly become smooth rings. After 48 hr hydration, the original Gaussian magnesiosilica grain size distribution became skewed with μ = 26 nm (1σ = 12.5 nm; range = 11–70 nm; mode = 17 nm). The positive skewness (S = 0.7) is consistent with grain coarsening. Adjoining rings begin merging together. The necklaces with irregular patches continue to pull together into amorphous ribbons and patches.

After 72 hr (357 K), the original silica smoke and silica balls with dehydration features that formed after 48 hr of hydration at this temperature are still present. Vestiges of the magnesiosilica smoke are also present, although the individual grains in necklaces are completely fused forming a tangled network of long sinuous ribbons. In general, the gradual process of coarsening of condensed grains to form ribbons, and the coagulation and collapse of the porous smoke to form the low-porous patches and "balls" observed after 48 hr, continues in this sample after 96 hr hydration at 357 K. Although coarsened in this sample, the silica smoke and patches, and the magnesiosilica smoke and dense spheres
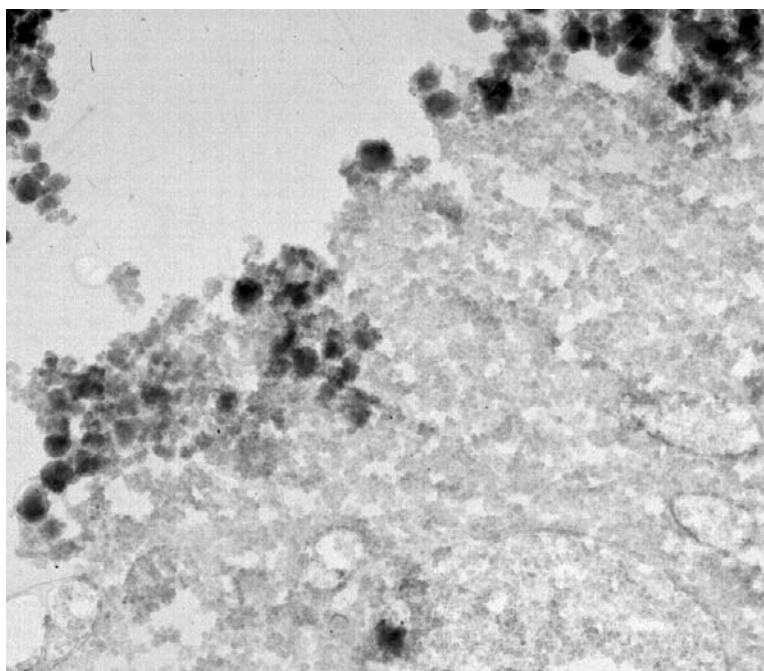
Fig. 2. Low magnification transmission electron microscope image of collapsed magnesiosilica smoke (light gray) surrounded by partially collapsed, coarsened silica smoke (dark) after hydration at 357 K for 96 hr. With continued hydration condensed silica smoke disappears and is precipitated as silica balls around magnesiosilica smoke domains. The field of view is 3.2 microns square. The gray background is the holey carbon support thin-film.

from the starting material, are still present, the silica and magnesiosilica ribbons are even more compact. The ribbons still define the original porous smokes.

The sample that was hydrated for 9.1 hr at 368 K shows the onset of the ultimate total collapse of the original smoke texture. The completely collapsed MgO-rich magnesiosilica smoke forms extensive contiguous sheets wherein the dense packing of ribbons induces a distinct foliation. Numerous pores from the rings are present in these sheets or layers. There are no traces of silica smoke. Silica spheres with a dehydration texture surround the sheets.

This is also true after hydration at 378 K for 3 hr when most of the magnesiosilica smoke forms large contiguous areas of densely packed material riddled with pores. The dense magnesiosilica spheres from the starting material persist, albeit with a somewhat increased size range, i.e., 50 to 285 nm (μ = 117 nm, 1σ = 47 nm). Small patches of tangled magnesiosilica ribbons and fused rings are still present. Both materials now contain abundant proto-phyllosilicates. Hydration for an additional 4.5 hr did not induce obvious changes in the sample treated at 378 K for 7.5 hr. A few traces of the original smoke with the low-MgO bulk composition remained.

In general, at 357 K (after 96 hr), 368 K, and 378 K, the original magnesiosilica smoke is overwhelmingly replaced by pervasive low-porous sheets ranging from 40 to 70 nm in size and balls of collapsed high-MgO smoke. The dense (low-porosity) balls range from 55 to 285 nm in diameter (μ =

117 nm; 1σ = 46.8 nm). High-resolution TEM imaging and SAED analyses show that the magnesiosilica and silica grains in the original open smoke, in collapsed domains of the starting material, and in the hydrated samples are typically amorphous. Rare lattice fringes (2.6, 1.9, and 1.2 nm; possibly tridymite) in massive silica spheres support short-range ordering.

Chemistry

The samples have unimodal MgO (wt%) distributions, except one hydrated at 378 K (7.5 hr) that has a bimodal distribution (Table 1). The distributions are either Gaussian or skewed with a negative or positive S value depending on hydration history. The data range in the starting material and the bimodal distribution provide hints to the chemical response during hydration. The reduced population for each sample includes both porous smoke and dense magnesiosilica domains that formed during hydration, possibly when the open smoke was pulled together by a liquid layer on the condensed grains (cf., Rietmeijer and Karner 1999). This is a gradual process, and transition textures exist. The composition of the recognizable original porous material in all hydrated samples ranges from 5–15 wt% MgO with a ~6 wt% MgO modal (bulk) composition, best fitting a lognormal distribution. The lower limit selected for data reduction is somewhat arbitrary, as porous material with as little as 2 wt% MgO does exist. The variations in bulk composition reflect variable relative proportions of silica and magnesiosilica

Table 1. Bulk compositions (MgO wt%) of the high-silica starting material as a function of hydration time and temperature. They are typically Gaussian distributions with listed values for the mean (μ) and one standard deviation (1σ). Skewness (S) and modal values are shown for non-Gaussian distributions; N is the number of analyses. Two samples hydrated at 357 K/72 hr were analyzed. The asterisk indicates the average values for (1) and (2).

Sample	Mean	1σ	Range	Mode	S	N
Condensed smoke	11.8	3.2	5–16	13.3	−0.5	19
357 K/48 hr	15.2	6.1	6–25	–	–	24
357 K/72 hr (1)	15.1	7.4	6–27	–	–	24
357 K/72 hr (2)	17.4	6.1	6–31	–	–	44
357 K/72 hr (*)	16.6	6.6	6–31	–	–	68
357 K/96 hr	8.7	2.7	5–15	7.6	0.4	33
368 K/9.1 hr	13.4	3.7	5–20	–	–	23
378 K/3 hr	21.0	4.7	8–29	22.3	−0.3	41
378 K/7.5 hr (bimodal)	10.7	1.9	8–13	–	–	8
	24.3	2.7	17–29	–	–	19

smokes in the material. The compositions of the compacted patches, sheets, and balls range from 16 to 31 wt% MgO and define a Gaussian distribution with μ = 21.7 wt% MgO (1σ = 3.5; N = 116). The condensed high-MgO magnesiosilica grain compositions were unaffected. These grains began gradual coagulation and coarsening.

Layer Silicates

Layer silicates are only found in fused magnesiosilica material with MgO = 22 ± 7 wt%. After 48 hr hydration at 357 K, long (50 to 75 nm) sinuous proto-phyllosilicates form tangled open networks (Fig. 3). These elongated features are 2 or 3 unit cells in thickness. Similar features, ~25 to ~50 nm long, of mostly two of these basal (001, hkl; Miller indices) layers are present after 72 hr at the same temperature. This sample shows the first dense network of randomly orientated, short (~10 to ~75 nm) and straight (spiky) proto-phyllosilicates that are typically one unit cell in thickness. Longer, mostly single-layer but also double-layered, proto-phyllosilicates follow the irregular outline of fused patches and pores therein or the perimeter of remnant condensed grains. The networks of spiky proto-phyllosilicates are unaffected by continued hydration to 96 hr at 357 K. The appearance and density of proto-phyllosilicates after hydration at 368 K (9.1 hr) and 378 K (3 hr) are indistinguishable from those formed at 357 K after 72 and 96 hr. In the former two samples, they are still overwhelmingly spiky, typically ~20 nm long, and only one or two unit cells thick. When longer, up to ~90 nm, they are often sinuous. Rare, small, stubby grains consist of 3, 4, or 5 well-ordered basal unit cell layers.

The mostly spiky proto-phyllosilicates show a complete range of (rare) crystallites with only a single 0.8-nm lattice fringe to crystallites of a single or two basal units with a fringe spacing of up to 2.4 nm. The lattice fringes define a multi-modal distribution, namely.: 1) 1.2 ± 0.06 nm; 2) 1.4 ± 0.08 nm; 3) 1.6 ± 0.05 nm; 4) 1.85 ± 0.06 nm; and 5) 2.0 ± 0.07 nm

and 2.3 ± 0.13 nm. The discontinuous stepped increase in d-spacing values is real within the error of measurement.

Well-ordered nanocrystals up to 50 × 5 nm and 30 × 15 nm with 0.9-nm lattice fringes occur in samples hydrated at 378 K (Fig. 4) and are also found in the sample hydrated for 48 hr at 357 K. They are extremely rare, which explains why they were not found in other hydrated samples.

A MgO-Rich Smoke: Starting Material

The starting material was produced in the Condensation Flow Apparatus. Broad-beam analyses indicate a bulk composition of 41 wt% MgO, while its calculated mean bulk composition is 47 wt%, which includes all magnesiosilica and MgO grains. Condensed silica grains that contribute ~10 wt% SiO_2 to the bulk composition make up the difference (Rietmeijer 1996).

Texture and Chemistry

The very open smoke contains four well-mixed, coarse-grained chemical entities. Listed in order of decreasing abundance, they are: 1) patches and dense agglomerations or clusters typically containing abundant electron-opaque grains; 2) dense clusters with only few such grains; 3) dense polycrystalline clusters; and 4) smooth featureless grains. The first type, patches and clusters, are, on average, 95 nm in diameter with a range from ~50 up to 175 nm. The lower limit is diffuse in a sense that some of the smaller entities in these patches and clusters that appear to be smooth grains may in fact be homogenized fused grain clusters. The individual entities then include smooth grains ranging from ~10 nm to 50 nm (μ = 24.7 nm; 1σ = 11 nm) and annular structures of fused, condensed grains (Fig. 5). Most rings have a hollow center, but in others, the core consists of a silica grain, which acted as an agglomeration center for condensing magnesiosilica grains into a flower-like arrangement (Rietmeijer et al. 2002b). In some rings, the original
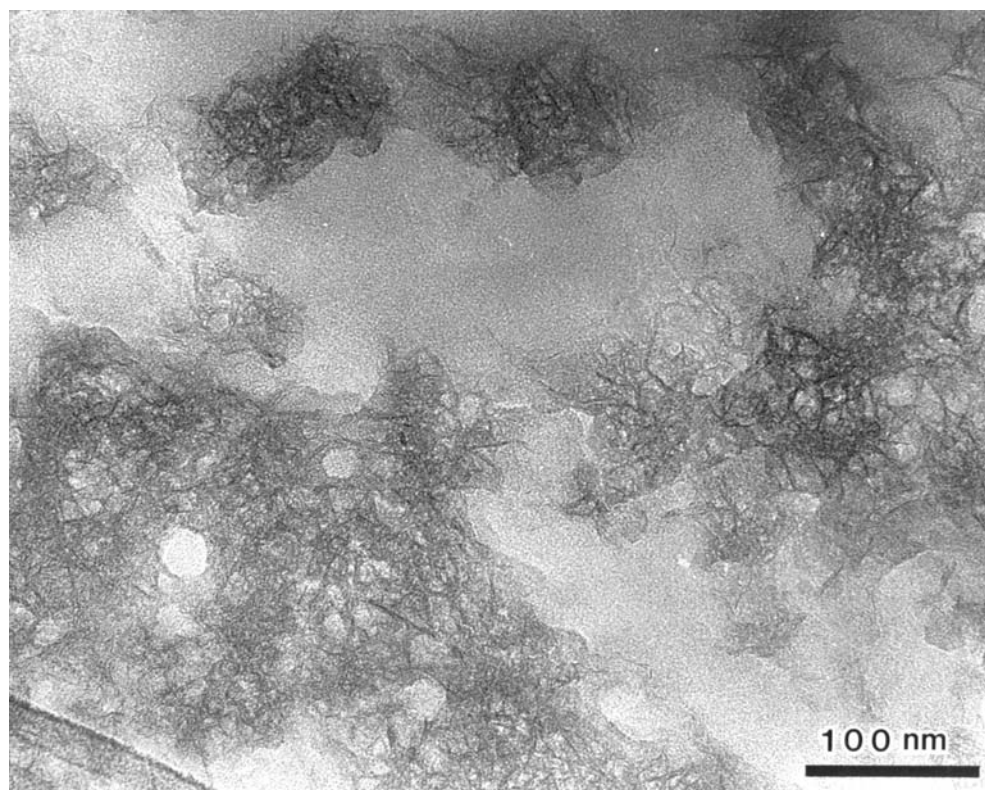
Fig. 3. Transmission electron microscope image showing the tangled open network of proto-phyllosilicates that formed in the magnesiosilica material with MgO = 22 ± 7 wt% in the sample hydrated at 357 K for 72 hr. This texture is typical for all hydrated Si-rich magnesiosilica smoke samples in this study. The gray background shows the embedding epoxy used for ultramicrotome sectioning and the holey carbon support thin-film.
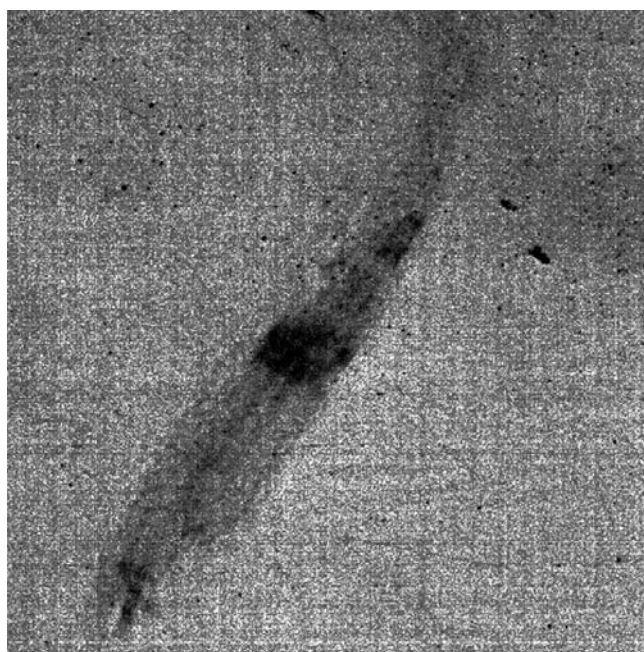
Fig. 4. Transmission electron microscope image of an extremely rare, well-ordered layer silicate nanocrystal (80 nm × 12 nm) formed in amorphous magnesiosilica smectite-dehydroxylate material after hydration above 357 K.

condensate grains are still recognizable, but typically, the individual grains in the rings have fused together, and the texturally homogeneous rings have acquired a smooth circumference. Some structures have a very large central hole and narrow annulus. Others are thick rings with a tiny hole. But, the most typical structure is in between these extremes. The mean annulus diameter is 29.7 nm (1σ = 11.85 nm) with a range of 15 to 60 nm. Formation of a typical annulus was determined by the original arrangements of the strands in the necklace texture of the condensed smoke. Smooth grains also formed by fusion of condensed magnesiosilica grains. The petrographic separation of rings and smooth grains does not carry significant genetic information. When used together for statistical analysis, these two textural magnesiosilica entities are, on average, 27.7 nm in size (1σ = 11.7 nm). The smooth grains and ring structures of fused grains could mix in the condensing vapor to be arranged in the dense clusters that dominate the sample. These clusters contain abundant electron-opaque inclusions (see below) and, occasionally, euhedral platy grains of olivine (EDS data) of up to ~50 nm in size. The grains and rings of fused condensates in the dense agglomerated clusters have a serpentine dehydroxylate composition of 51 wt% MgO (Table 2).

The dense clusters (~75 up to 275 nm) also consist of smooth grains (μ = 22.2 nm; 1σ = 7.9 nm; range = 6–35 nm)
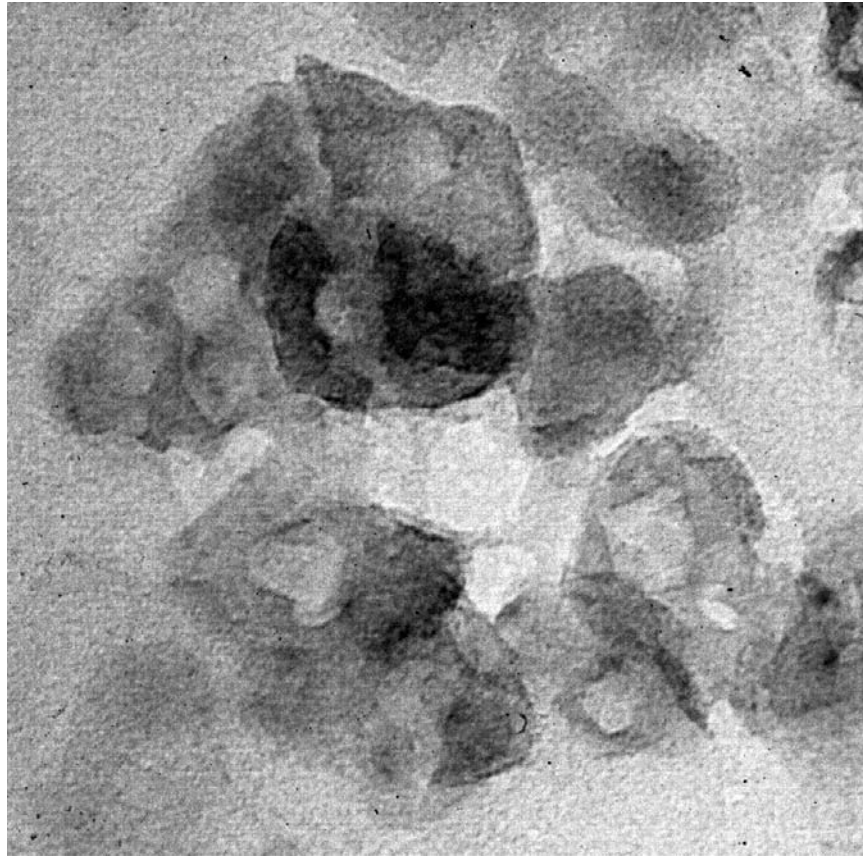
Fig. 5. Transmission electron microscope image showing annular structures of fused, individually condensed smectite-dehydroxylate grains in the MgO-rich magnesiosilica smoke that was used as the staring material for hydration experiments. The dark ring in the center is 57 nm in diameter; the hollow center is 19-nm across. The gray background is the embedding epoxy used for ultramicrotome sectioning and the holey carbon support thin-film.

Table 2. Compositions (MgO wt%) of magnesiosilica material in the condensed and hydrated high-MgO samples. The compositions define Gaussian or skewed normal distributions.

Sample	Starting material			423 K/22 hr		573 K/74 hr
Mean	24.8	51.0	89.0	35.5	86.2	33.5
Std. dev (1σ)	6.3	8.3	7.1	8.4	2.8	6.8
Range	12–34	35–73	79–94	15–52	84–91	12–43
Mode	28.0	–	–	37.2	–	37.3
Skewness	–0.5	–	–	–0.2	–	–0.6
N	33	101	4	67	5	69

and similar ring structures (μ = 23.8 nm; 1σ = 12.5 nm; range = 4–55 nm). The lower limit of the range for the rings shows that there is no fundamental distinction between these rings and the smooth grains with a mean diameter of 23.1 nm (1σ = 10.6 nm) in these clusters. The Student t-test shows that the mean for the grain and ring entities in these dense clusters with a smectite dehydroxylate composition of 24.8 wt% MgO (Table 2) is smaller than the mean diameter of the serpentine dehydroxylate entities. The smectite-dehydroxylate grain clusters also contain electron-opaque inclusions (see below), but they are significantly less abundant than in the serpentine dehydroxylate material. There are also slightly elongated, platy euhedral grains ~30 to ~50 nm in size. Some smooth

smectite-dehydroxylate grains have a rim of concentric, circular (proto) fringes with a ~0.9-nm lattice spacing (Fig. 6).

Compact Mg-rich clusters up to 300 × 180 nm have a mean composition of ~95 wt% MgO. They are agglomerations of magnesiosilica material, 89 wt% MgO (Table 2), and pure MgO (EDS analysis) platy periclase grains 2 to 40 nm in size. Other rounded grains in these clusters are 8 to ~15 nm in size. The composition of this magnesiosilica material matches that of the high-MgO metastable eutectic in the MgO-SiO$_2$ phase diagram (Rietmeijer et al. 2002b).

Pure silica occurs as mostly rounded and subhedral grains, some with a texture indicating fusion of condensed grains. Pure silica also forms platy euhedral grains. The
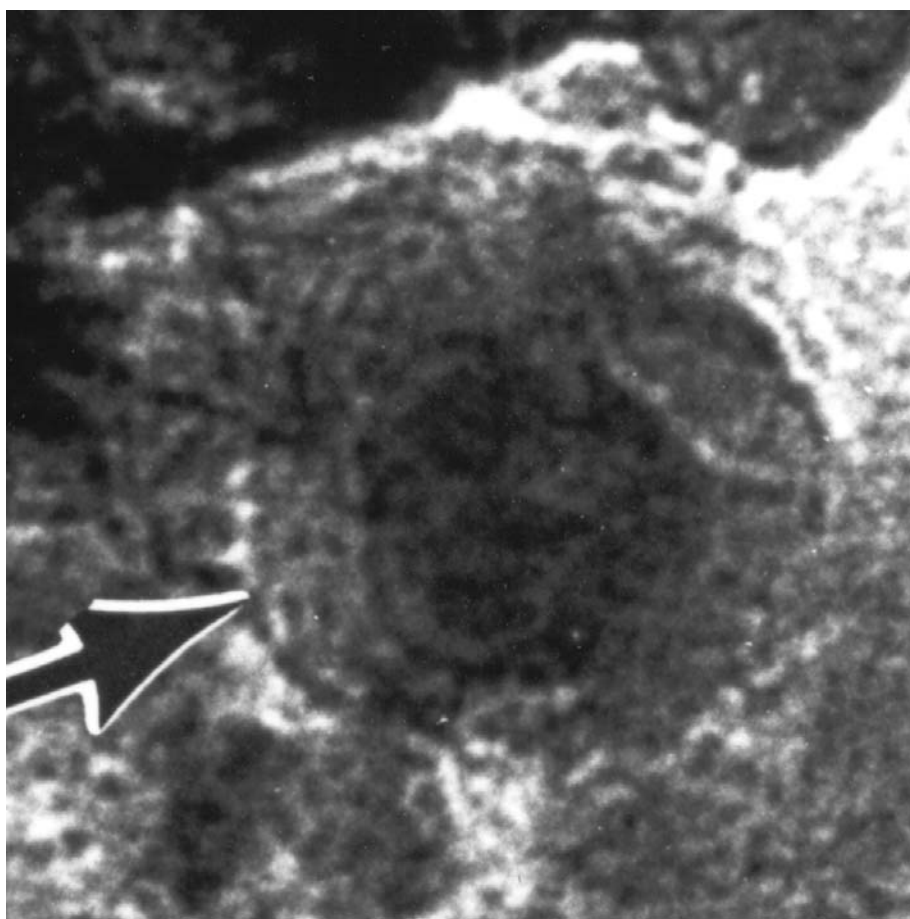
Fig. 6. Transmission electron microscope image showing of concentric circular (proto) fringes (arrow) along the periphery of a smooth smectite-dehydroxylate grain (15 nm in diameter) in the MgO-rich magnesiosilica smoke used as the starting material for hydration experiments.

average grain size is 30.5 nm (1σ = 14.1 nm) with a range of 9 to 65 nm. Coarse-grained silica forms patches of fused smoke and isolated grains that are well mixed with the magnesiosilica clusters.

Electron-Opaque Inclusions

Electron-opaque inclusions occur as the silica core of rings. They are also randomly scattered, in widely variable proportions, in the dense clusters of serpentine and smectite dehydroxylate grains (Fig. 7). In both occurrences, crystallographic twinning indicates that some are probably tridymite. The smallest, predominantly silica, inclusions range from 2 to 8 nm with a mean diameter of 4.6 nm (1σ = 1.9 nm); larger inclusions up to 13 nm show a Gaussian size distribution with μ = 9.9 nm (1σ = 1.6 nm). They, as well as the platy grains, include olivine, pyroxene, and silica.

Crystallographic Properties

Periclase (MgO), forsterite (Mg_2SiO_4), enstatite ($MgSiO_3$), and SiO_2 polymorphs are the only possible stoichiometric phases in the anhydrous MgO-SiO_2 system. The condensed solids show a remarkable degree of

crystalline development that was not observed previously in other condensed magnesiosilica smokes (Rietmeijer et al. 1986, 2002b). But, when nanocrystals occurred in amorphous, non-stoichiometric, metastable solids, it was determined that kinetically controlled crystallization favored the metastable formation of forsterite plus tridymite instead of enstatite (Rietmeijer et al. 1986, 2002a; Thompson and Tang 2001).

The d-values, shown as a function of the metastable eutectic host composition, indicate that the opaque domains in fused and agglomerated smectite dehydroxylate condensates are tridymite and forsterite (Table 3). The presence of enstatite cannot be excluded, but lacking diagnostic d-values, it is not uniquely identified (Table 3). It is different for nanocrystals in the serpentine dehydroxylate condensates that include forsterite, tridymite, and possibly enstatite. These minerals suggest the operation of two different reactions, namely: 1) the typical formation of forsterite plus silica that is independent of the metastable eutectic composition; and 2) the decomposition, $Mg_3Si_2O_7 \rightarrow 2MgSiO_3 + MgO$, observed here for the first time in metastable magnesiosilica material. Crystallization of the amorphous MgO-rich magnesiosilica
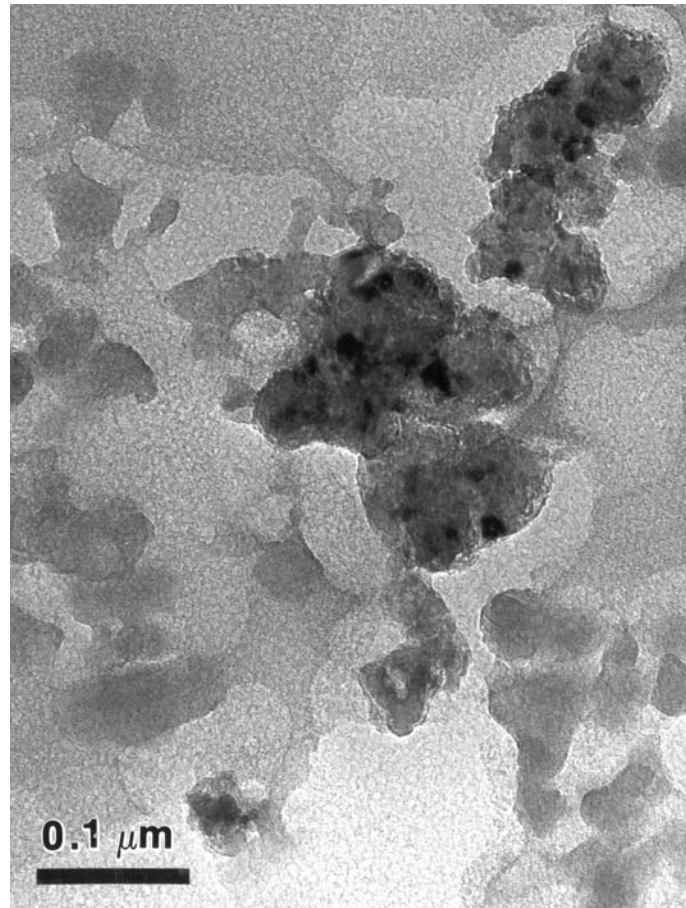
Fig. 7. Transmission electron microscope image showing dense clusters of condensed MgO-rich magnesiosilica material with randomly scattered, electron-opaque inclusions. This sample served as the starting material for hydration experiments. The gray background is the embedding epoxy used for ultramicrotome sectioning that tore loose around the clusters and the holey carbon support thin-film.

Table 3. d-values (nm) based on polycrystalline ring SAED patterns for condensed materials with: (1) smectite dehydroxylate; (2) serpentine dehydroxylate; and (3) high-MgO magnesiosilica metastable eutectic compositions. Data from the J.C.P.D.S. X-ray diffraction files: #7–74 (forsterite), #19–768 (enstatite), # 14–260 (tridymite), and #6–615 (periclase).

Observed			d-spacing (hkl)			
(1)	(2)	(3)	Forsterite	Enstatite	Tridymite	Periclase
	0.65			0.63 (210)		
	0.60	0.60	0.599 (001)			
	0.51		0.510 (020)	0.517 (001)		
	0.44		0.430 (110)	0.441 (020)	0.453 (0018)	
	0.42					0.421 (100)
	0.39		0.388 (021)		0.383 (209)	
0.38					0.380 (2010)	
0.37			0.372 (101)		0.361 (2012)	
0.33	0.35	0.33	0.350 (111)	0.330 (121)	0.328 (2015)	
0.31		0.31		0.315 (221)	0.316 (216, 1120)	
	0.30	0.30	0.300 (121); 0.292 (002)		0.300 (2110)	
		0.29		0.287 (610)	0.283 (304, 2114)	
		0.28	0.277 (130)	0.282 (511)	0.276 (308, 1028)	
0.26	0.26		0.251 (131)	0.253 (131)	0.259 (2025,1030)	
0.25	0.25		0.246 (112)		0.249 (3016)	
	0.24	0.24	0.238 (200)			0.243 (111)
	0.21	0.21	0.216 (220, 211)	0.211 (630)		0.211 (200)

metastable eutectic material (Table 2) produced periclase and forsterite in the reaction $Mg_{13}SiO_{15} \rightarrow 11MgO + Mg_2SiO_4$.

MgO-Rich Sample Hydrated at 423 K for 22 Hr

Texture and Chemistry

A few remnants of the original units remain, but the most striking feature is that the patches and dense agglomerations of serpentine dehydroxylate material with the electron-opaque grains and the pure silica smoke have all but vanished. The original open texture of the dense magnesiosilica clusters of fused smooth grains and ring structures has collapsed and forms a coherent mass of magnesiosilica material of 35.5 wt% MgO plus interspersed pockets of 86 wt% MgO (Table 2) and abundant tabular grains. The magnesiosilica material is highly porous mainly because the holes of the original rings were preserved during hydrous collapse. Pores smaller than ~40 nm are generally spherical. The larger pores tend to have an elongated, hexagonal shape or a square cross section. Their shape is probably an annealing feature from hydration at this temperature. Intermixed non-porous pockets are probably remnants of the original smooth grains, although their size range, from 10 nm to 150 nm, is much wider than for the original grains. Also, their mean diameter, 45 ± 17 nm, is larger than in the starting material. The magnesiosilica (MgO = 35.5 wt%) material is an amorphous thin foil with a multitude of holes. It contains scattered, typically equant nanocrystals ranging from ~4 nm to 40 nm with a modal dimension of 4.6 nm and a high abundance of proto-phyllosilicates and tabular grains.

Tabular Grains

The tabular and rare pillbox-shaped grains have an average aspect ratio of 0.23 ± 0.12 (1σ) ranging from 0.06 (ribbon-like) to 0.5 (stubby grains). They are 30 nm up to 80 nm × 325 nm in size. There is no preferred size. Individual grains are generally scattered randomly. They may form parallel stacks of several grains or random clusters up to 500 nm in size or be confined to a narrow zone (Figs. 8, 9, and 10). The grains, ~95 to 100 wt% MgO, are highly susceptible to thermal interaction with the incident electron beam that causes dehydration and amorphization. First, there is the formation of broad, occasionally sinuous, bands parallel to all major crystallographic planes, then the formation of a checkerboard pattern of domains with parallel lattice fringes with holes at the domain corners, and ultimately, a fully amorphous material with numerous holes (Fig. 10). The initially single-crystal SAED patterns show evidence for randomization of crystallites and the formation of a new phase. All d-values <0.3 nm listed in Table 4 are averages for a range of diffraction maxima forming cloud-like clusters in the initially single-crystal patterns. The d-values >0.30 nm are based on well-defined diffraction maxima only in the SAED pattern of the Mg-rich tabular grains with up to 5 wt% SiO_2 (Table 4). The diffraction data show a mixture of brucite + periclase in pure MgO grains and a mixture of brucite + periclase + forsterite in the Mg-rich tabular grains. The minerals support dehydration of silica-bearing brucite to periclase + forsterite by the reaction $(Mg[OH]_2 + 0.05SiO_2)_{solid\ solution} \rightarrow 0.9\ MgO + 0.05Mg_2SiO_4 + H_2O$. Dehydration and formation of periclase + forsterite are artifacts.
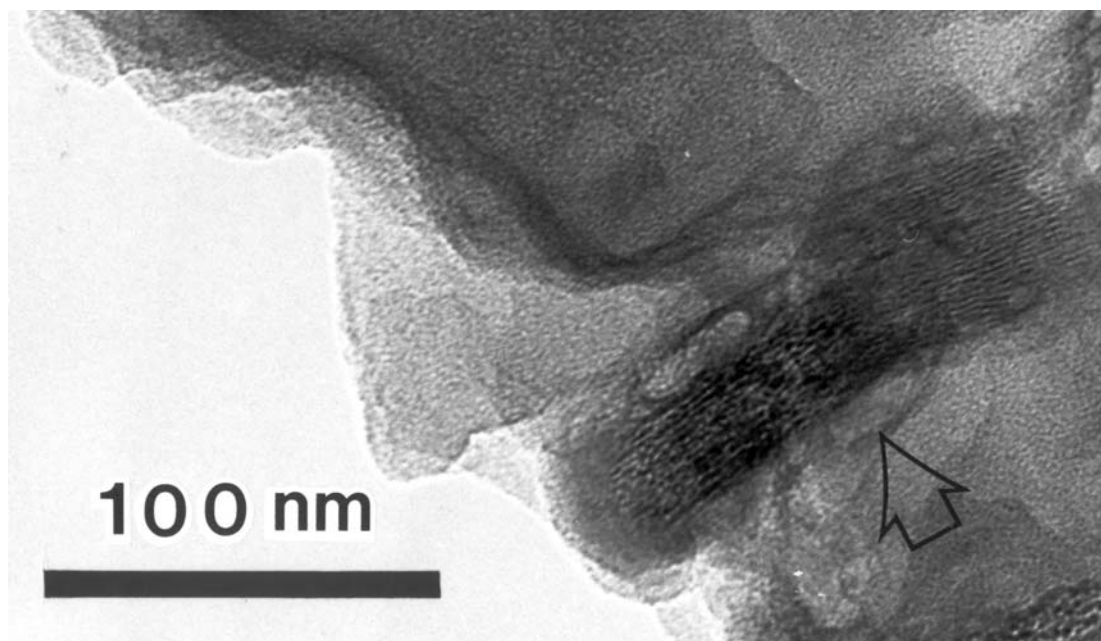
Fig. 8. Transmission electron microscope image of a brucite single-crystal grain formed in the hydrated magnesiosilica smoke matrix after 22 hr of hydration at 423 K. The gray background is the embedding epoxy.
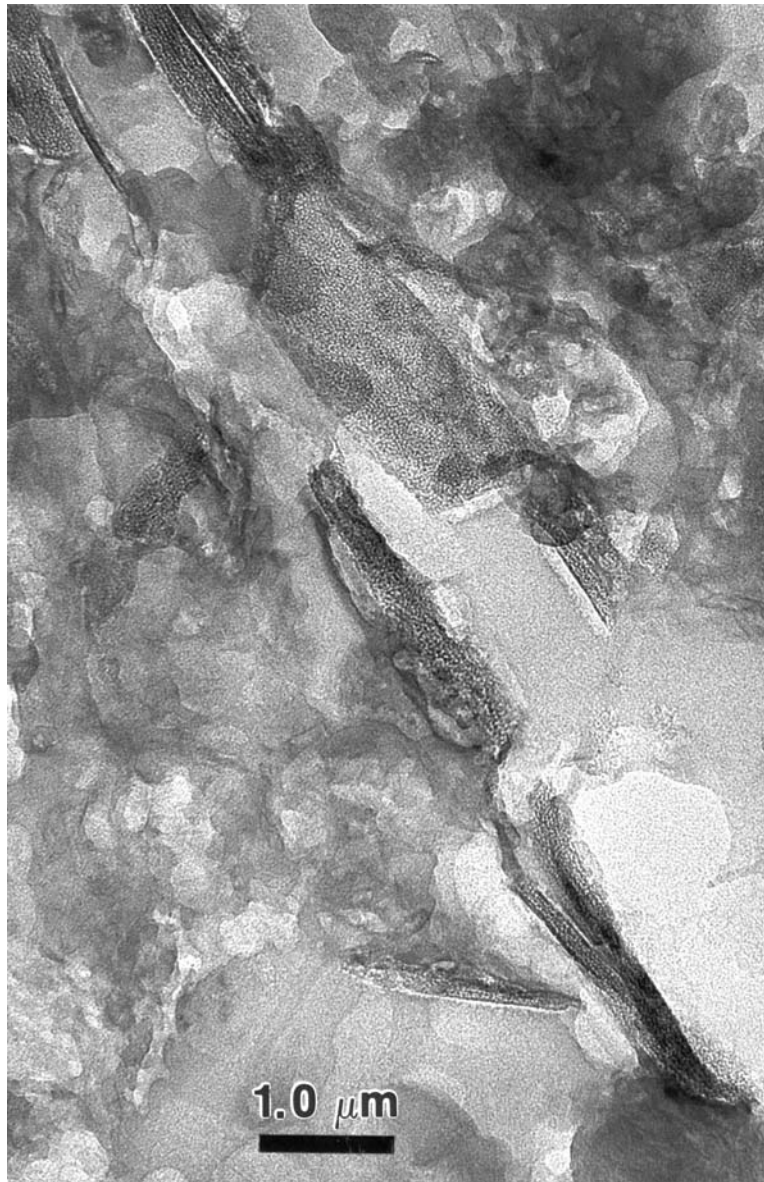
Fig. 9. Transmission electron microscope image showing a narrow zone of brucite grains in the hydrated magnesiosilica smoke matrix after 22 hr of hydration at 423 K. The sample was displaced along the zone of brucite grains during ultramicrotome sectioning. The gray background is the embedding epoxy.

Proto-Phyllosilicates

Proto-phyllosilicates form typically spiky but also sinuous crystallites that can be up to 145 nm long, "flowing" around pores. The spiky crystallites form concentric layers in annular structures and around pores. But, they are generally randomly oriented into dense tangled masses (Fig. 11). When individual crystallites with mostly one or two, and occasionally up to five, unit cell layers of thickness occur side-by-side, they form highly turbostratic nanocrystals. The spiky crystallites show a complete range from only a single basal layer of 1.0 nm (rare) to crystallites of two or three, and up to eight, unit cell layers. Their lattice fringes define a stepped pattern, namely: 1) 1.2 ± 0.1 nm; 2) 1.4 ± 0.09 nm; 3)

1.6 ± 0.07 nm; 4) 1.9 ± 0.08 nm; and 5) 2.0 ± 0.09 nm and 2.2 ± 0.08 nm. A few well-ordered grains of about 50×25 nm in size have 0.6 nm lattice fringes.

MgO-Rich Sample Hydrated at 573 K for 74 Hr

Texture and Chemistry

The sample is a mixture of three texturally distinct materials, namely: 1) highly-porous, amorphous magnesiosilica material with proto-phyllosilicates; 2) a dense material with large sinuous layer silicates generally showing turbostratic layer stacking; and 3) pockets of large, densely-packed, well-ordered layer silicates (Figs. 12 and 13). Proto-
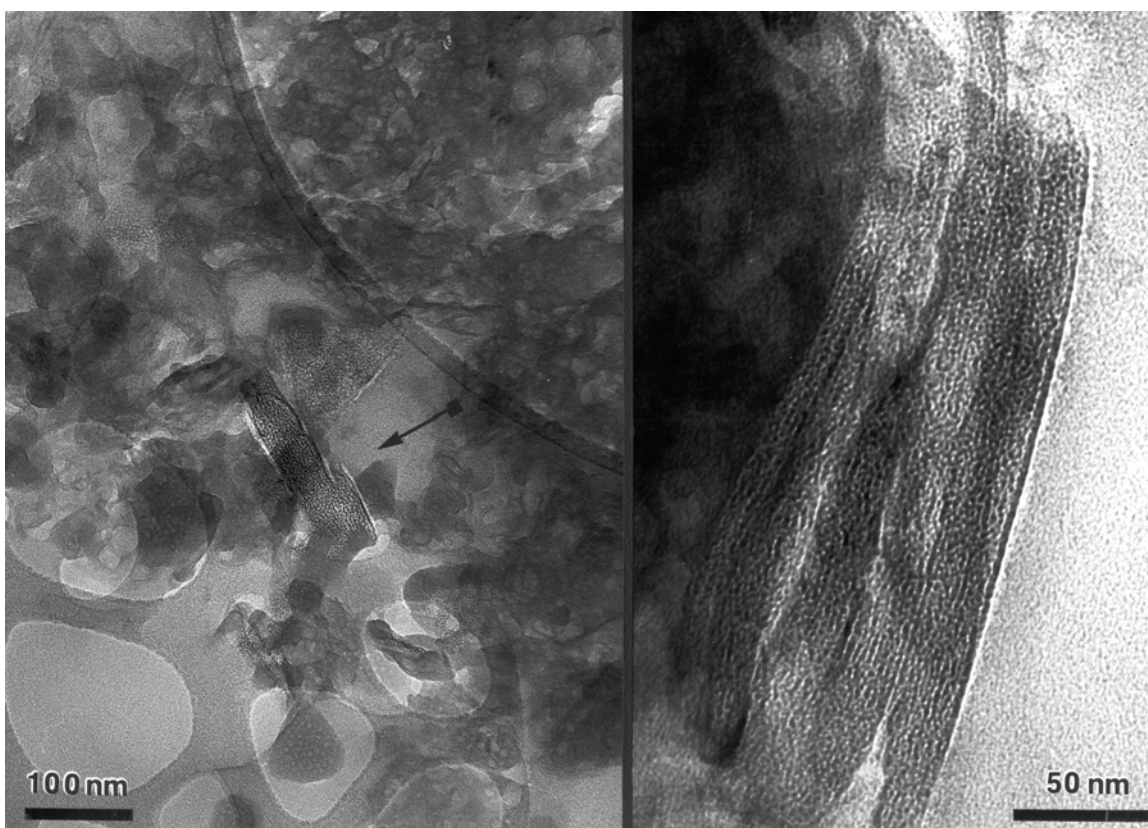
Fig. 10. Transmission electron microscope image on the left showing two individual brucite grains in the hydrated magnesiosilica smoke matrix after 22 hr of hydration at 423 K. They show almost complete amorphization after exposure to the incident electron microbeam. The arrow in this image indicates the grain shown on the right that consists of four parallel sub-units. The gray background shows the embedding epoxy and the holey carbon support thin-film.

Table 4. d-values (nm) based on single-crystal SAED patterns for pure-Mg and Mg-rich tabular grains. There is a complete transition from single-crystal brucite to a polycrystalline mixture of brucite + periclase (± forsterite) to an amorphous pseudomorphic replacement. Data are from the J.C.P.D.S. X-ray diffraction files: #7–239 (brucite), #6–615 (periclase), and #7-74 (forsterite).

| Observed | d-spacing (hkl) | | |
	Brucite	Periclase	Forsterite
0.61			0.599 (001)
0.35			0.350 (111)
0.30	0.298 (110)	0.315 (100)	0.300 (121); 0.292 (002)
0.28	0.2725 (100)		0.277 (130)
0.245		0.243 (111)	0.246 (112)
0.24	2.365 (101)		0.238 (200)
0.21		0.211 (200)	0.216 (220, 211)
0.16	0.157 (110)		0.162 (133); 0.159 (152)
0.15	0.149 (111)	0.149 (220)	0.150 (004)
0.12	0.119 (004); 0.118 (202)		

phyllosilicate appearance and textures in this sample are indistinguishable from those in the sample hydrated at 423 K/ 22 hr. Its bulk composition (Table 5, column 1) defines a skewed normal distribution with a modal value of 37.3 wt% MgO. The Student's t-test shows that the means for this population and the one for the sample hydrated at 423 K/22 hr (Table 2) do not support the idea that these two samples are different. But, in the sample hydrated at 573 K (74 hr), it can be shown that two different populations define the skewed distribution, that is: 1) a Gaussian distribution (μ = 38 wt% MgO) for the highly porous, amorphous material with a tangled proto-phyllosilicate network; and 2) a skewed, normal distribution (μ = 27.8 wt% MgO) dominated by larger layer silicate grains (Table 5). The combined data using a small data
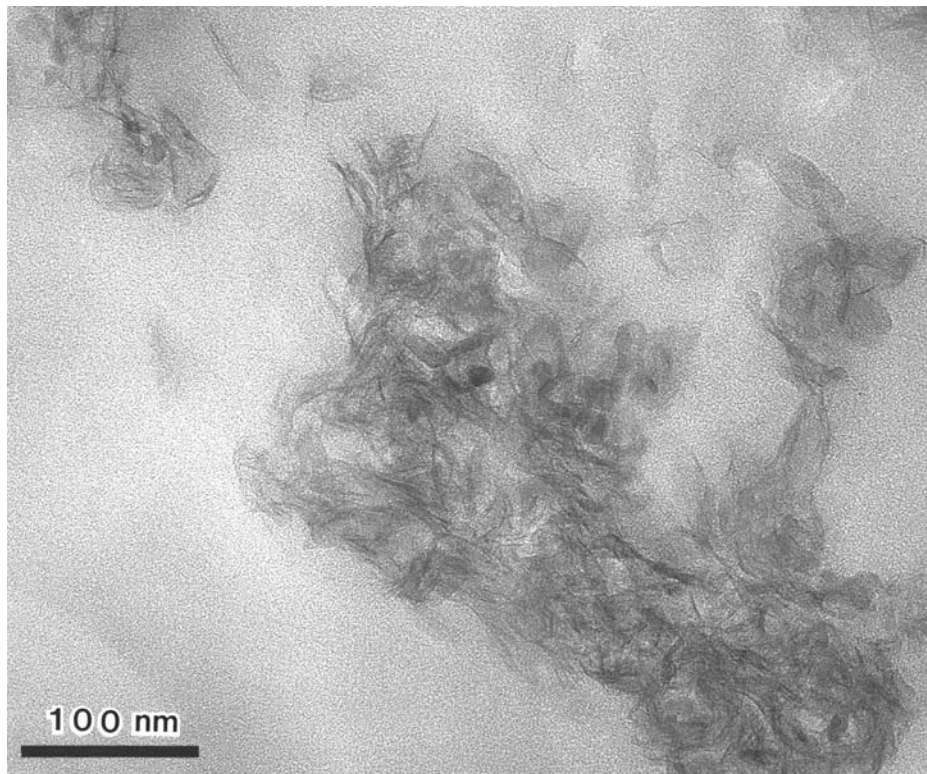
Fig. 11. Transmission electron microscope image of a dense, tangled mass of randomly oriented proto-phyllosilicates in the hydrated MgO-rich magnesiosilica matrix after hydration at 423 K and 22 hr. The gray background is the embedding epoxy.
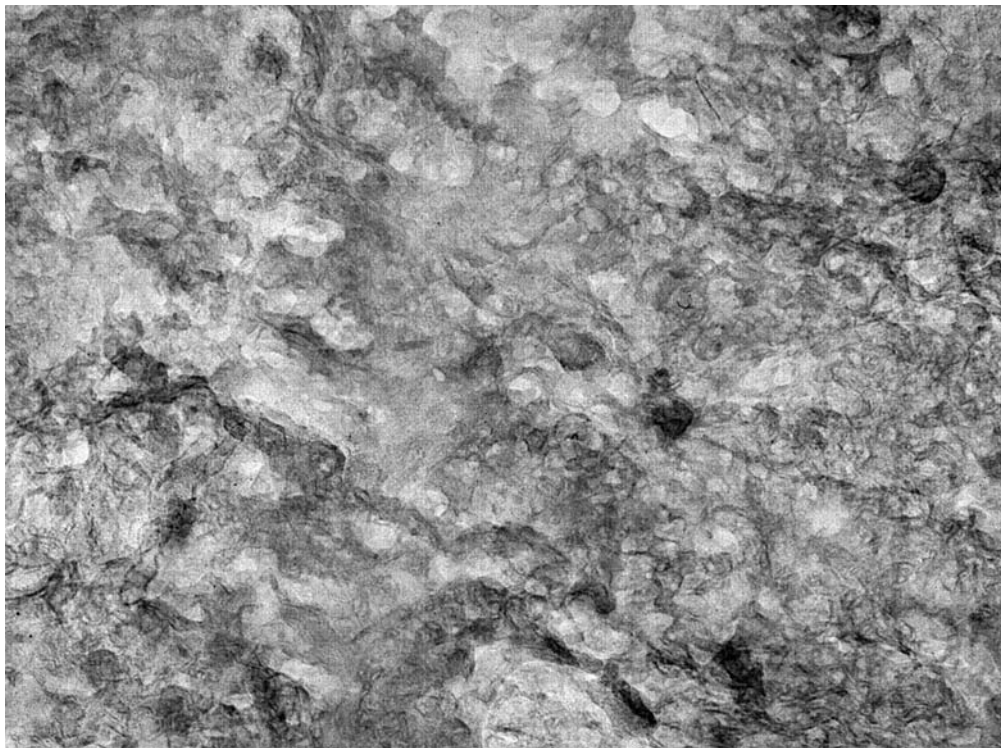
Fig. 12. Low magnification transmission electron microscope image of the highly porous, amorphous magnesiosilica matrix with densely packed proto-phyllosilicates in magnesiosilica material hydrated at 573 K for 74 hr. The field of view is 870 nm × 630 nm. The gray background is the embedding epoxy with large holes after microtome sectioning.
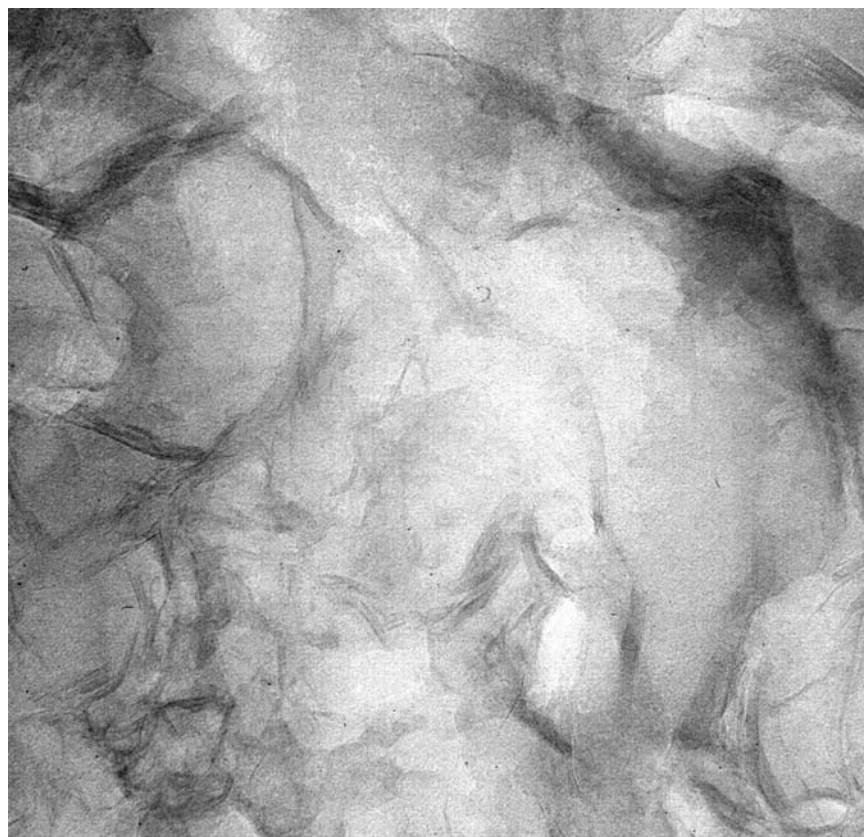
Fig. 13. Transmission electron microscope image of turbostratic and well-ordered layer silicates, both with 1.0-nm lattice fringes, in the amorphous magnesiosilica matrix after hydration at 573 K for 74 hr. The gray background is the embedding epoxy.

Table 5. Compositions (MgO wt%) for the magnesiosilica material in the sample hydrated at 573 K for 74 hr (column 1, see Table 2) subdivided on the basis of the predominance of proto-phyllosilicates (I), the larger layer silicates (II), and the combined data for (I) + (II).

	Bulk	(I)	(II)	Combined
Mean	33.5	38.0	27.8	34.1
Std. dev (1σ)	6.8	2.9	8.5	7.5
Range	12–43	32–43	12–36	12–43
Mode	37.3	–	34.1	37.2
Skewness	–0.6	–	–0.7	–0.7
N	69	18	11	29

set defines a population that is indistinguishable from the larger data set. The tabular brucite grains were not found in this sample, which could be an artifact of sample selection for TEM analyses. However, low-magnification TEM imaging should readily reveal these easily recognizable grains when present in the hydrated smoke. With a high level of confidence, it can be stated that brucite was not present in this sample.

Proto-Phyllosilicates and Layer Silicates

The straight (spiky), sinuous, and curved proto-phyllosilicates are similar to those in the sample hydrated at 423 K for 22 hr but with a markedly higher incidence of spiky proto-phyllosilicates with one or two 1.0-nm unit cell layers. Rare, ordered crystallites are 5 or 6 1.0-nm unit cell layers in

thickness. The spiky crystallites tend to be longer than in the other hydrated Si-rich and Mg-rich samples. Here, they are mostly ~15 nm to ~75 nm long with an average length of 35 ± 15 nm. Their aspect ratio ranges from 0.03 to 0.11 ($\mu = 0.06$; $1\sigma = 0.02$). Much smaller spiky crystallites still abound.

Densely packed ragged flakes of layer silicates with turbostratic layer stacking and well-ordered nanocrystals occur in micron-sized, non-porous domains with a smectite dehydroxylate composition, 27.8 wt% MgO (Table 5). The basal unit cell layer spacing is 1.0 nm. The aspect ratios of the well-defined and well-ordered crystals range from 0.06 to 0.24 (i.e., ribbon-like) ($\mu = 0.13$; $1\sigma = 0.05$). They are ~175 to ~500 nm long. The ragged layer silicates have aspect ratios ranging from 0.09 to 0.53 ($\mu = 0.20$; mode = 0.15; $1\sigma = 0.1$).

The ragged crystals are ~80 up to ~310 nm long. These properties could indicate a gradual transition from proto-phyllosilicates, to ragged turbostratic layer silicates, and to well-ordered layer silicates.

DISCUSSION

The critical properties that drive the response of condensed magnesiosilica smokes during hydration at increasingly higher temperatures and longer times include: 1) the metastable eutectic composition of the amorphous condensates; 2) the original smoke texture, i.e., porosity; and 3) the ultrafine, nanometer-scale grain sizes of all entities in the smokes. The kinetically controlled condensation experiments discussed here proceed in two distinct stages to dissipate the thermal energy, namely: 1) condensation proper; and 2) autoannealing that might induce post-condensation modification of dust settling in the vapor and of condensates on the collector. Some textures such as compact clusters or ring structures could form during deposition and residence on the collector. But, ring structures with a silica core also form when condensed dust resides in the condensing vapor (Rietmeijer et al. 2002b). In previous thermal annealing studies of condensed MgSiO smokes, it was demonstrated that the texture of the original starting material could have a dramatic impact on the chemical and mineralogical, and therefore spectral (IR), evolution of the sample during heat treatment (Fabian et al. 2000; Rietmeijer et al. 2002b). Nuth et al. (2002) argued that some caution is required when applying the results of condensation and thermal annealing experiments to reaction rates of processes that occur in active comet nuclei and circumstellar dust. Careful petrological analyses of analogue samples are useful to constrain the mineralogical and chemical changes during thermal annealing or hydration.

Metastable Eutectic Dust

Kinetically controlled, gas-to-solid condensation occurs far removed from thermodynamic equilibrium, but it is not a chaotic process. Condensation in Al-SiO-O_2-H_2, Mg-SiO-O_2-H_2, and Fe-SiO-O_2-H_2 vapors invariably produced mixed AlSiO, FeSiO, and MgSiO grains (<20 to 50 nm) with predictable chemical compositions. This behavior in the binary systems Al_2O_3-SiO_2 (Rietmeijer and Karner 1999), MgO-SiO_2 (Rietmeijer et al. 2002b), and the pseudo-binary system FeO/Fe_2O_3-SiO_2 (Rietmeijer et al. 1999b) is possible because they have at least two eutectic points. This topology allows for at least one metastable eutectic point (Nuth et al. 2002; Rietmeijer and Nuth 2000a). The grain compositions define metastable eutectics in the phase diagram (Nuth et al. 1998, 2002; Rietmeijer et al. 2000). These metastable eutectic grains are typically amorphous solids that will be very reactive during changes in the physiochemical environment.
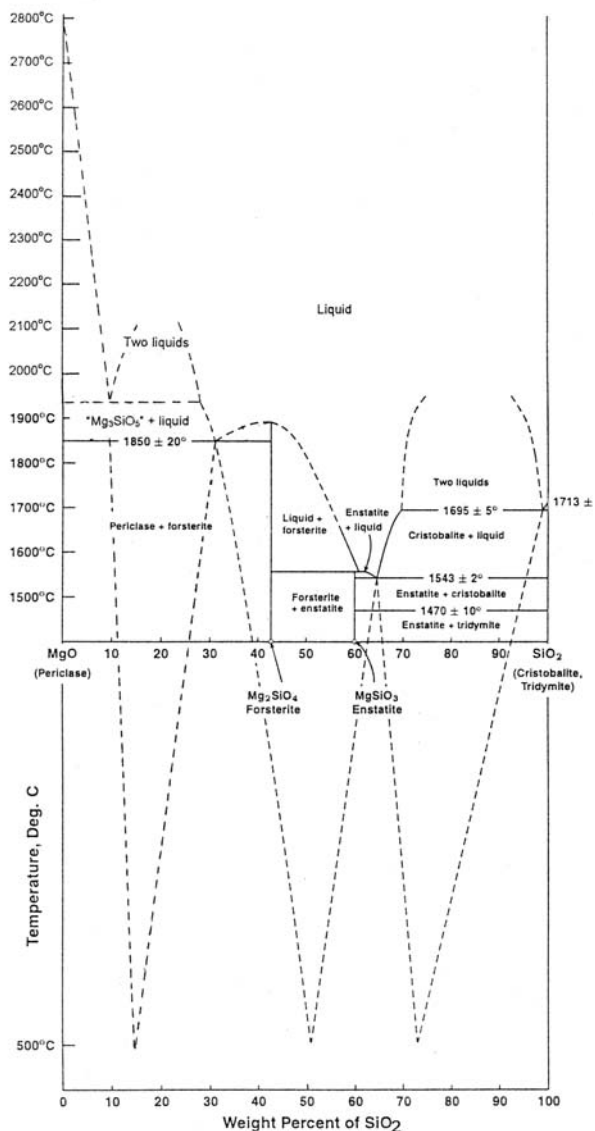
Fig. 14. The MgO-silica phase diagram showing the three metastable eutectic compositions of individual magnesiosilica grains produced by kinetically controlled gas-to-solid condensation of a Mg-SiO-H_2-O_2 vapor. With increasing MgO content, the eutectic points are smectite, serpentine, and high-MgO dehydroxylates. The positions of the metastable eutectics in the diagram reflect the measured compositions and the nominal quench temperature of the experiment. Being a metastable phenomenon, they cannot fit a unique temperature. This figure was modified after Rietmeijer et al. (2002b). The upper part is the original phase diagram published by E. G. Ehlers in *The interpretation of geological phase diagrams,* 1972, San Francisco: W. H. Freeman, 280 p.

The co-condensed pure oxide grains are invariably crystalline, namely, tridymite (a high-temperature SiO_2 polymorph), Fe_3O_4, γ-Fe_2O_3 (maghémite), or periclase.

Metastable eutectic grains in the MgO-SiO_2 system have three distinct compositions, namely: 1) smectite-dehydroxylate, $Mg_6Si_8O_{22}$; 2) serpentine-dehydroxylate,

$Mg_3Si_2O_7$; and 3) high-MgO magnesiosilica grains (Fig. 14). The amorphous serpentine and smectite dehydroxylate grains have MgO/SiO_2 ratios identical to those of the layer silicate minerals serpentine and saponite (a smectite-group mineral). As a result of this unique chemical property of the hydration of condensed grains, e.g., $Mg_6Si_8O_{22} + 2H_2O = Mg_6Si_8O_{20}(OH)_4$ (saponite), only the availability of water will be the critical, rate-limiting reactant.

This observed metastable eutectic behavior is a fundamental property of kinetically controlled gas-to-solid condensation wherein these "dissipative structures" arise when their state of disorder is able to persist for some length of time (Rietmeijer and Nuth 2000a; Rietmeijer et al. 2000). This behavior was found in different binary systems wherever formation of metastable eutectic compositions was possible (Nuth et al. 2002). But, it was also shown not to occur when the phase diagram did not allow for metastable eutectic behavior, even though the physical conditions would have promoted this behavior (Rietmeijer et al. 1999a). The bulk composition of the condensing gas phase does not affect metastable eutectic behavior in a binary system.

The estimated bulk composition of the SiO_2-rich smoke is ~12 wt% MgO. The measured bulk composition of the MgO-rich starting material is 41 wt% MgO. In a third magnesiosilica smoke, the bulk composition is ~26 wt% MgO (Rietmeijer et al. 2002b). All three condensed smokes show metastable eutectic behavior, though the relative proportions of condensed grains with the three possible metastable eutectic compositions is a function of the bulk composition of the condensing gas phase, that is, magnesiosilica grains in the silica-rich smoke only occur as smectite-dehydroxylate. Pure silica condensed, but no MgO grains were observed. In the smoke with an intermediate bulk composition, the condensed grains have: 1) smectite, 2) serpentine, and 3) high-MgO magnesiosilica metastable eutectic compositions in decreasing order of relative abundance. These compositions are found in the MgO-rich smoke discussed here, but serpentine dehydroxylate grains are the most abundant of the three followed by smectite dehydroxylate grains and scarce high-MgO magnesiosilica metastable eutectic solids. The intermediate and high-MgO smokes also contained pure silica and MgO condensates. The formation of metastable eutectic compositions is a fundamental property, but the relative proportions of these condensates are sensitive to the gas phase composition. This implies that post-condensation modification will follow a general pattern of behavior.

Proto-Phyllosilicates in Condensed Magnesiosilica Smokes

The high probability that water was present in the condensation chamber cannot be ignored. The SiO molecule is the dominant silica species in the vapor. It is an efficient reducing agent for reactions such as $SiO + MgO = SiO_2 + Mg^0$

(Nuth and Hecht 1990) or $SiO + H_2O = SiO_2 + H_2$, which control the amount of water that could form during condensation. If so, condensed metastable eutectic magnesiosilica grains might show evidence for hydration. Indeed, Rietmeijer and Nuth (2001) found a hydrated zone that was from one and up to four ~0.9-nm unit cell layers thick along the perimeter of a few amorphous, 10–50 nm-sized grains in a condensed magnesiosilica smoke. This up to 3.4-nm wide zone is only found on smectite dehydroxylate grains. Similar zones were found in the smooth smectite dehydroxylate grains of the MgO-rich starting material discussed here (Fig. 6). This particular proto-phyllosilicate, probably talc, occurrence is a surface energy related feature. It is distinctly different from the water-saturated conditions used during the post-condensation hydration experiment.

Autoannealing of Condensed Magnesiosilica Materials

Crystallization of amorphous grains with a stoichiometric mineral composition is common in these condensed smokes (Rietmeijer and Karner 1999; Rietmeijer et al. 1999b, 2002b). Electron-dense areas occurred among grains with metastable eutectic compositions, particularly when their larger-than-average grain size or their presence in dense agglomerations indicated that they are fused original condensates. The stochastic nature of the processes during condensation proper and the grain growth when settling in the condensing gas and on the collector, thus, provide a variety of conditions for the formation of domains with stoichiometric mineral compositions among the metastable eutectic condensates. The domains, such as in the MgO-rich starting material, are typically a few nanometers in size and always less than ~15 nm (Rietmeijer et al. 2002b). The number of domains in smectite dehydroxylate material is generally very small. They had a high abundance in the serpentine dehydroxylate material of the MgO-rich smoke. During mild post-condensation thermal annealing, the tridymite and forsterite inclusions, and all pure oxide minerals, undergo solid state amorphization when going though the glass transition temperature, which results in completely amorphous materials (Rietmeijer et al. 1999b). This process is also expected to occur at the temperatures of the initial hydration reactions.

Chemical Changes During Hydration

Leaching and Precipitation

All materials in the condensed smokes are metastable and, thus, are highly reactive solids. The fluffy SiO_2-rich smoke is a random mixture of magnesiosilica and pure silica smokes, both with the typical necklace texture of grains <<100 nm in diameter. Silica also occurs as irregular patches and massive clusters. After hydration for 48 hr at 357 K, most of the condensed silica has disappeared. Silica, opal-A spheres are now surrounding the pure magnesiosilica smoke.

The radial shrinkage cracks in these spheres indicate loss of water during freeze-drying of the samples. Viewed in the proper textural context, the compositions as a function of progressing hydration (cf., Table 1) support aqueous dissolution and leaching of the metastable porous silica smoke from the original, intermixed high-silica MgSiO smoke and the subsequent precipitation of this material. The reaction between water and the silicon-oxygen network of condensed silica produces a weak silicic acid that is the main means to transport dissolved silica. The pH values that controlled dissolution and precipitation in the hydration experiment are unknown. The experiment showed that hydration is an efficient process for the chemical, and resultant physical, separation of pure silica and magnesiosilica condensates with implications for aqueous alteration in CI parent bodies (Rietmeijer and Nuth 2000b). Hydrothermal modification was limited to the magnesiosilica smoke that had acquired its metastable smectite dehydroxylate composition (MgO = 22 ± 7 wt%) during kinetically controlled condensation.

Chemical Homogenization

The MgO-rich smoke is yet another example of the efficiency of an aqueous fluid to erase the original chemical heterogeneity of a vapor-condensed magnesiosilica smoke. It is a mixture of the three possible metastable eutectic magnesiosilica materials (Table 2), periclase, and silica. It is dominated by serpentine dehydroxylate condensates. Yet, the dominant magnesiosilica material in both hydrated samples contains 33–35 wt% MgO (Table 2) that, at 423 K after 22 hr, is accompanied by brucite and some silica. Both of the latter phases were absent after 74 hr at 573 K. The serpentine-dehydroxylate patches, dense agglomerations and silica-rich materials had apparently dissolved. The overall highly porous texture of both hydrated samples resembles the smectite-dehydroxylate material of the starting material.

This combination of texture and original chemical heterogeneity suggests the simultaneous dissolution of silica, which is evident in the hydrated high-SiO_2 smoke, plus serpentine dehydroxylate condensates, and the subsequent co-precipitation of silica onto highly porous, unaffected smectite dehydroxylate material. For convenience, the reaction $Mg_3Si_2O_7 + 3SiO_2 + nH_2O = 3MgO.5SiO_2.nH_2O$ is written using a stoichiometric formula for the reagents, which is not strictly correct for these amorphous materials, while the product follows the convention for amorphous solids. It is readily appreciated that the reaction product contains 40 wt% MgO, which is higher than was listed in Table 2 for the hydrated magnesiosilica materials. However, the distributions of proto-phyllosilicates and well-ordered layer silicates in the sample hydrated at 573 K for 74 hr show that these populations for the hydrated sample compositions are a composite of a Gaussian distribution, $\mu = 38$ wt% MgO, and a skewed normal distribution, $\mu = 27.8$ wt% MgO (Table 5).

The mean value of 38 wt% MgO for the highly porous material matches the composition of the reaction products shown above. Is this composition arbitrary or predictable? Hydration was the first opportunity for the condensed smokes of metastable eutectic solids to move toward thermodynamic equilibrium via a series of kinetically controlled metastable intermediary stages. It seems likely that the new composition reflects an attempt to reduce metastable eutectic disorder in the samples. In the MgO-rich smoke discussed here, the relative amounts of magnesiosilica material, brucite, and remnant silica were such that dissolution at higher temperatures and longer times did not effectuate a change in the newly formed composition.

Comparison of Magnesiosilica Compositions

A test of population means for the smectite dehydroxylate compositions in both starting materials shows that the mean in the MgO-rich sample ($\mu = 24.8$ wt% MgO; Table 2) is larger than the mean in the SiO_2-rich starting material ($\mu = 21.7$ wt% MgO; Table 1). When assessing this result, it should be appreciated that the silica-rich end of the population range was difficult to assess. This test for population means of smectite dehydroxylate compositions in the MgO-rich starting material (Table 2) and the material with well-defined layer silicates ($\mu = 27.8$ wt% MgO; Table 5) shows that there is no evidence that they are from two different populations. The analysis shows that smectite dehydroxylate condensates survived hydration for 74 hr at up to 573 K in the MgO-rich starting material.

Testing population means in the MgO-rich starting material (Tables 2 and 5) shows that the population mean, $\mu = 38$ wt% MgO (Table 5), of the hydrated magnesiosilica material is greater than that for the condensed smectite dehydroxylate grains but smaller than for the serpentine dehydroxylate grains. The skewed normal distributions for magnesiosilica materials in the MgO-rich samples (Table 2) suggest that ,after hydration for 22 hr at 423 K, this population is also a combination of condensed smectite dehydroxylate grains and this new population of hydrated material. The composition of this new population is due to hydration of the original serpentine-dehydroxylate and high-MgO metastable eutectic condensates, silica and MgO.

Proto-Phyllosilicates and Well-Ordered Layer Silicates

Formation

The formation of hydrated silicates requires transport through and diffusion of molecular water into the metastable eutectic magnesiosilica grains to interact with the silicon-oxygen network of these materials. The interaction that carries water into the amorphous material can be written Si-O-Si + H_2O = SiOH + HOSi (Doremus 1995; Doremus and Perera 1991). The OH groups will readily react with amorphous metastable magnesiosilica material that already

has an appropriate Mg/Si ratio. Thus, the local availability of water in the samples should be a rate-controlling step in the hydration experiments as a function of variable porosity.

We make a strict distinction between proto-phyllosilicates and well-ordered layer silicates. Proto-phyllosilicates are a kinetically controlled response during the hydration of anhydrous precursors that already had proper stoichiometric phyllosilicate Mg/Si ratios. Well-ordered layer silicates probably formed at close-to-equilibrium growth conditions, although we cannot prove this assumption. The proto-phyllosilicates and well-ordered nanocrystals in the hydrated SiO_2-rich smoke formed in the condensates with a smectite dehydroxylate composition of 22 wt% MgO. Thus, diffusion was either not necessary or very limited, and hydrated silicates formed quickly as soon as water became available. The newly-formed hydrated magnesiosilica material (μ = 38 wt% MgO) in the MgO-rich samples is silica-saturated compared to serpentine dehydroxylate. It favors the formation of smectite minerals and talc rather than serpentine (Martin and Fyfe 1970). The Mg/Si ratio of this material does not match these hydrated silicates, which means that the appropriate Mg/Si ratio had to be created. We suggest that proto-phyllosilicate appearances and random distributions in dense tangled networks suggest that the right Mg/Si ratios resulted from a process resembling spinodal decomposition, that is, by the formation of continuous wave-like decomposition of a homogeneous solid solution into regions of (slightly) different compositions but very similar structures. Such spinodal behavior would be an alternative form of metastable behavior in materials because it does not involve an activation energy barrier for nucleation of the new phase (Putnis and McConnell 1980). This process offers a rapid response that we submit determined proto-phyllosilicate formation in fully hydrated, amorphous magnesiosilica material. In this regard, the IR data for the samples are inconclusive because: 1) the spectra did not show any "fully" hydrated features for proto-phyllosilicate species that developed at different rates; and 2) there is considerable overlapping of IR features in the spectra. The randomly oriented proto-phyllosilicates yielded a highly disordered, amorphous, hydrated magnesiosilica material.

Proto-Phyllosilicate Identification

The compositional constraints limit the choice of possible minerals to saponite, $Mg_6Si_8O_{20}(OH)_4.nH_2O$, kerolite or talc-hydrate, $Mg_6Si_8O_{20}(OH)_4.2H_2O$, with typically turbostratic basal layer stacking, talc ($Mg_6Si_8O_{20}[OH]_4$), and stevensite, which is an interstratification of saponite and talc. Sepiolite, $Mg_8Si_{12}O_{32}.12H_2O$, is an unlikely candidate because of its complex structure. For saponite, the d_{001} spacing value ranges from ~1 to 2.1 nm, while this spacing for dehydrated saponite is similar to the $d_{(001)}$ = 0.9 nm of talc and $d_{(001)}$ = 1 nm of kerolite. The observed lattice fringes range from 1.0 nm for dehydrated saponite or kerolite to 2.4 nm. The stepped range of the d-values >1.0 nm supports saponite with different degrees of hydration due to increasing water (vapor) pressure, which is different from sorption of water on external grain surfaces (Newman 1987). This process was studied for a number of swelling clays, but data for Mg-saponite are scarce (Newman 1987). The observed saponite lattice fringe distributions show no correlation with hydration time and temperature nor do we have reason to believe that variable lattice fringes are experimental artifacts of exposure to the incident electron beam. The well-ordered nanocrystals, d_{001} = 0.9 nm, are probably talc. The co-occurrence of talc, kerolite, and saponite with discontinuous spacing of lattice fringes highlights the variable availability of water that was most likely controlled by local porosity of collapsing smokes. The tangled proto-phyllosilicate networks occur in the highly porous magnesiosilica materials.

Textural Modification

The key to appreciating post-condensation smoke modification is that nothing happens as long as the individual condensed grains are preserved in the porous necklace texture. This feature is well-illustrated in two thermal annealing studies on differently prepared magnesiosilica smokes. In one study, the IR signature signified a stall phase wherein there were no detectable mineralogical changes during continued heat treatment, but the time-temperature relationship induced continued changes in the IR spectra of the samples both before and after the stall was achieved (Hallenbeck et al. 1998). In similar experiments, Fabian et al. (2000) found no evidence for this stall phase, although Thompson and Tang (2001) did achieve a stall phase. The TEM data showed that the smallest entities believed to represent the original condensates were ~50 nm in size (Fabian et al. 2000). Similar data for a magnesiosilica smoke that showed this stall phase revealed that the condensed grains were ~10 nm and that the stall phase marked a fusion process whereby these grains formed ~50 nm-sized entities (Rietmeijer et al. 2002a). The samples documented by Fabian et al. (2000) could have been formed when they were already past the stall phase due to the manner in which they were produced.

The magnesiosilica smoke in the SiO_2-rich starting material used in the hydration experiments resembled the smoke that showed the stall phase. The MgO-rich smoke with its dense clusters of auto-annealed serpentine and smectite dehydroxylate condensates resembled the smoke that did not show a stall phase. In other words, the isolated condensed grains in a porous necklace texture must first collapse before there is sufficient contact area to allow chemical and mineralogical evolution. Therefore, it will take longer for such modifications to occur. On the other hand, when condensed grains that were already processed into larger entities are subsequently subjected to post-condensation processing, mineralogical and chemical modification will proceed much

faster and lead to coarser-grained reaction products. Rietmeijer and Karner (1999) showed that a thin, initial melt layer on individual condensed grain surfaces is an efficient whetting agent to pull the individual entities of a porous smoke together. Similarly, water in the hydration experiments was an efficient agent to pull the condensed grains or autoannealed dense clusters into a compact material. Although the high porosity of the original starting materials was increasingly reduced during progressive hydration, it never became zero. In fact, the hydrated layers or pockets of compacted original and newly formed, modified, smectite dehydroxylate materials still show considerable porosity inherited mostly from the original ring structures. This porous texture was conducive to the free movement of water through the samples.

As a consequence of these textural modifications, the hydrated MgO-rich samples are expected to contain larger and better-developed proto-phyllosilicates and larger, well-ordered layer silicates than the hydrated magnesiosilica material of the SiO_2-rich starting material. As was seen in the former starting material, proto-phyllosilicate growth occurs via the addition of basal fringes by parallel stacking and when growing proto-phyllosilicates begin to merge more-or-less along their basal planes into larger entities with highly turbostratic stacking of the original crystallite layers. This process requires some continuity of the amorphous matrix wherein they grow. The smaller size of proto-phyllosilicates in the hydrated silica-rich smoke compared to those in the MgO-rich smoke was determined by the initial grain sizes of the entities that pulled together into dense pockets during hydration, that is, the difference between small, condensed grains and large, dense, condensed grain clusters, respectively. The density and distribution of pore spaces is also critical in this regard. While more pore space facilitated the availability of water, it restricts the volume for growth as shown by the long sinuous proto-phyllosilicates and those flowing around or lining individual pores. Ragged layered grains with turbostratic stacking could develop from growing proto-phyllosilicates because of the continuity of the matrix. Pockets of very low-porosity and non-porous magnesiosilica pockets are well-mixed with the porous materials that are host to the tangled proto-phyllosilicate networks. These original textures offered protection during hydration to high temperatures for long times to allow the survival of pure smectite dehydroxylate material wherein well-ordered, dehydrated smectite or kerolite was formed at 573 K/74 hr. Similarly, the few well-ordered serpentine crystals formed in rare, non-porous remnants of collapsed serpentine dehydroxylate grain clusters.

Implications of the Hydration Experiments

Interplanetary Dust Particles

Anhydrous and hydrated aggregate IDPs are not fundamentally different particles. Both contain the same fundamental building blocks, and the only difference is porosity (Rietmeijer 1998, 2002a). Our experiments support a previous conclusion that chondritic aggregate IDPs are uniquely different from the components in any collected meteorites, and thus, they are different from parent bodies that are not sources of these meteorites (Mackinnon and Rietmeijer 1987). The hydration experiments show clearly that the collapse of an anhydrous porous smoke will be inevitable during hydration. By analogy, water acting as a whetting agent of the fine-grained constituents in anhydrous porous aggregates will cause the particle to become a low- or non-porous (partially) hydrated aggregate IDP. Zolensky and Barrett (1994) suggested that phyllosilicates in (partially) hydrated IDPs are a unique indicator of an asteroidal origin. Yet, the uniqueness of this indicator remains in doubt until it is proven that water, e.g., as a thin interfacial layer for hydrocryogenic alteration below the ice melting point, could not exist in active comet nuclei (Rietmeijer 2002a).

Saponite is the dominant layer silicate in the majority of hydrated aggregate IDPs that frequently also contain minor serpentine (Zolensky and Lindstrom 1992; Zolensky and Barrett 1994). The hydration experiments showed that the formation of saponite and talc is independent of the Mg/Si ratio of the anhydrous precursor particle that might have contained both condensed serpentine and smectite dehydroxylate grains. Hydration will shift the fully hydrated precursor bulk compositions toward magnesiosilica compositions that are in between those of the condensed, metastable eutectic dust. Consequently, smectite minerals (saponite) and talc will be the most abundant hydration products, and depending on the original pre-hydration texture, small amounts of serpentine will also form. The hydration experiments confirm the observed hydrated silicate mineralogy of collapsed aggregate IDPs that, by inference, still preserve vestiges of the condensation processes of the dust accreted in IDP parent bodies.

Zolensky and Lindstrom (1992) also reported ultrafine-grained periclase in a saponite-bearing aggregate IDP, which so far is the only particle wherein this oxide was found. They suggested that periclase formed: 1) during atmospheric entry heating by dehydration of pre-existing brucite, although the presence of brucite was not explained; or 2) during condensation in the solar nebula under distinctly non-chondritic, highly Si-depleted conditions that inhibited the condensation of forsterite. Neither explanation was satisfactory. The condensed dusts from magnesiosilica vapors with atomic Mg/Si ratios of 0.52 (range: 0.2–1.0) and 1.04 include pure MgO and high-MgO metastable eutectic magnesiosilica grains. Thus, there is no need to invoke extreme solar nebula compositions to explain minor amounts of periclase in primitive extraterrestrial materials. For comparison, we note that the Mg/Si (at.) ratio in dust at comet Halley was 0.54 (Jessberger et al. 1988). This ratio is 0.55 for coarse-grained, low-iron ferromagnesiosilica principal components in aggregate IDPs (Rietmeijer 1998, 2002a).

Schramm et al. (1989) reported a bulk ratio Mg/Si (at.) = 0.82 for hydrated "chondritic smooth" IDPs (CI value is 1.08). The experiments further show that hydration at high temperatures will ultimately erase all traces of condensed MgO or brucite formed earlier during hydration. Periclase survived in a (partially) hydrated aggregate IDP, but the hydration experiments suggest that brucite or periclase will not be present in CI chondrites unless thermally processed, in which case, MgO could be formed from pre-existing carbonates (Tonui et al. 2003). They could be accessory phases in the matrix of unequilibrated ordinary chondrites.

Comets

The ultimate goal of laboratory dust analogue studies is to understand the formation of the original circumstellar dust, the efficiency of dust modification processes in primitive protostellar bodies, e.g., comet nuclei and asteroids, and the nature of the reaction products. These successful and maturing experiments use combinations of sophisticated analytical tools, e.g., infrared spectroscopy and transmission electron microscopy, to determine the properties of the original and processed dust analogues (Nuth et al. 1998, 2002; Rotundi et al. 2002). For example, but without an attempt to be comprehensive, such laboratory studies, including this study, define condensation and thermal annealing of Fe- and Mg-silicates (Carrez et al. 2002; Fabian et al. 2000; Hallenbeck et al. 1998; Rietmeijer et al. 2002a; Thompson and Tang 2001) and carbon dust analogues (Jäger et al. 1999; Rietmeijer et al. Forthcoming; Rotundi et al. 1998) as well as hydration of condensed silicates. This unique niche of experimental petrology also recognized that time is not on our side and that, therefore, high temperatures will be needed to achieve meaningful results within our lifetimes. Thus, the results of a thermal annealing or hydration experiment will be cast in the form of an Arrhenius equation that will include experimentally obtained values for the pre-exponential term and activation energy.

Samples discussed here were part of such a study wherein the pre-exponential term and activation energy were determined for hydration of SiO_2-rich magnesisosilica smokes using the ratio of "the mass of hydrated silicate" to the "mass of anhydrous Mg-SiO" in the samples as a function of time and temperature (Nelson et al. 1987). The resulting Arrhenius relationship may then be used to predict kinetic hydration rates at other temperatures but within a reasonable extrapolation of the experimental conditions (Nelson et al. 1987).

In this paper, we make a distinction between proto-phyllosilicates and "layer silicates" because the former could form without nucleation, while the latter might not. Although the ragged turbostratic layer silicates could be an intermediate mode of occurrence, we have no evidence that these layer silicates undergo a probably reconstructive transformation to well-ordered, dehydrated smectite or kerolite. Recognizing this distinction is germane to appreciating the results of the hydration experiments and their relevance to layer silicates in primitive meteorites wherein both occur, often side-by-side (Brearley and Jones 1998). When applying the results to the formation of hydrated silicates in the matrix of carbonaceous chondrites and cometary dust, Nelson et al. (1987) made the caveat that the products of the hydration reactions remained the same. The data presented here show that, indeed, there is only one product in the form of tangled, overwhelmingly saponite, proto-phyllosilicate networks with the occasional larger nanocrystals. Still, the saponite proto-phyllosilicates contained variable amounts of water. Nelson et al. (1987) assumed that the formation of hydrated silicates would require (activation) energy, which has now been found not to be the case, and they hypothesized that growth of the 11.5-micron feature required "a secondary alteration product." The present study shows no evidence for two different phases of hydrated silicate formation as a function of kinetic hydration. Nelson et al. (1987) suggested that the strength of the 11.5-micron feature in the spectra might indicate the local elimination of "amorphous" character in the silicate. It would happen when simple bond rearrangements were catalyzed by the presence of water causing the formation of a less disordered, more highly cross-linked silicate. The original description by Nelson et al. (1987) describes the spontaneous (no activation energy), i.e., spinodal formation of proto-phyllosilicates in a hydrated amorphous magnesiosilica material with a metastable eutectic composition. The TEM data show a correlation between the amount of proto-phyllosilicates and the temperature and time of hydration.

Nelson et al. (1987) considered diffusion of Mg^{2+} or OH^- in the condensed solids as possible rate-limiting steps. Yet, the local availability of these species is probably a more severe constraint that will be determined by sample porosity. The TEM data show that while the initial porous smoke structure collapses, holes of the original rings remain open to water flow. While overall porosity will decrease as the experiment progresses, the OH^- diffusion rate (Mg^{2+} is not important) will increase, and these two processes will control the hydration history of the samples. Given that neither the composition nor appearance of hydrated silicates changed during the experiment, the rate equation developed by Nelson et al. (1987) is most probably a measure of available pore space and OH^- diffusion. If this interpretation is correct, this hydration study has important implications for the collapse of porous, anhydrous, aggregate IDPs to compact, hydrated, aggregate IDPs in active comet nuclei and carbonaceous chondrite parent bodies. The experimental data then trace the micro-textural changes in comet nuclei before "macro-textural" changes such as those simulated in the KOSI experiments (e.g., Kömle and Steiner 1992).

The experimentally obtained reaction rates (Nelson et al. 1987) predict that significant hydration on a time scale of days already occurs at 300 K, that is, the time leading up to and following perihelion for most comets. Depending on the

exact values of thermal conductivity in a cometary nucleus, including dust-ice ratios, the experiments by Kömle and Steiner (1992) determined that transient pockets of liquid water could exist in an active comet nucleus. A measured 400 K surface temperature of comet Halley (Emmerich et al. 1986) would suggest that liquid water might well be available for the hydration of amorphous, metastable, eutectic ferromagnesiosilica dust but may not be available for the hydration of crystalline silicates.

During the recent Leonid storms, which were debris from comet Tempel-Tuttle (Jenniskens et al. 2000; Rietmeijer 2002b), OH emission lines were observed in spectra of these meteors. These emissions could arise from ablating organic materials, the silicate fraction, or both. The TEM and IR analyses of hydrated analogues reported here show that: 1) hydrated amorphous magnesiosilica dust can be present in active comet nuclei; and 2) saponite proto-phyllosilicates can be important repositories of water in comet nuclei. Without getting involved in the arguments over how comets may have played a role in the origin of life on Earth, we note that the silicate fraction of comets should be considered when calculating the delivery of water to the early Earth. Ice-free nuclei could well be fully hydrated material and would, therefore, carry significant quantities of water.

In a search for compositional trends in rock-forming elements in comet Halley, Fomenkova et al. (1992) concluded that brucite or periclase or possibly both minerals could be among the dust grains ejected from this comet. Fomenkova et al. (1992) quoted the earlier report by Zolensky and Lindstrom (1992) of periclase in one aggregate IDP. Periclase is a very rare natural mineral, which gives some credence to a very tenuous link of this one IDP to a cometary source. The kinetically controlled condensation in Mg-SiO-H_2-O_2 vapors (Rietmeijer et al. 2002b), and the starting materials reported here, supports a notion that, under certain strict conditions, a particular mineral could be a tracer for an origin in a primitive solar system body.

Circumstellar Dust

The ISO spectra for several stars, including some O-rich stars, show features at 48 μm and 91 μm that have yet to be identified but that could indicate the presence of hydrated silicates (Molster et al. 2002). These authors correctly noted that the presence of layer silicates in stellar outflows poses a bit of a problem because layer silicate formation will require the presence of water. The hydration experiments show that highly disordered dust of tangled saponite proto-phyllosilicate networks are readily formed in condensed amorphous dust with a metastable silica-rich magnesiosilica composition without the requirement of an activation energy for nucleation. There is also the possibility that sub-micron grains of well-ordered saponite and talc might form during hydration of these materials. These newly defined boundary conditions for saponite and talc formation might provide a previously unrecognized niche for hydrated silicates in circumstellar environments or stellar outflow sources where at least some water vapor or OH is present.

The properties of condensed MgSiO-smokes, including the starting materials used for the hydration experiments, provide constraints on the nature and evolution of dust around Herbig Ae/Be stars (Bouwman et al. 2001; Nuth et al. 2002) and in comets (see above). The constraint imposed by the absence of water of hydration in stellar outflows noted by Molster et al. (2002) may be alleviated when considering the role that comets play in the processing and evolution of protostellar dust (Hill et al. 2001). Firmly establishing that the 48 μm and 91 μm ISO features are caused by highly disordered proto-phyllosilicate-rich magnesiosilica dust would provide support for the early evolution of proto-comet nuclei that involve sequences of (small) parent body modification and disruption. Such a scenario was implied as part of the proposed hierarchical process of early solar system dust accretion (Rietmeijer 2002a).

CONCLUSIONS

The magnesiosilica smokes used in the hydration experiments were produced by kinetically controlled gas-to-solid vapor phase condensation, which gave them the unique properties that determined their mineralogical and chemical evolution during hydration. The properties driving the response during hydration at increasingly higher temperatures and longer times are: 1) the metastable eutectic compositions of amorphous condensates; 2) the porous smoke texture; 3) the ultrafine, nanometer grain sizes of all entities in these smokes; and 4) water supersaturation throughout the time-temperature regimes of hydration. The last-listed property produced the conditions wherein proto-phyllosilicates could form without activation for nucleation. Their formation and subsequent growth was entirely determined by the availability of water as a function of the distribution and density of inherited pore spaces and the textural continuity of magnesiosilica materials with mostly smectite dehydroxylate compositions. Depending on the initial condensing gas composition, the hydration history will involve significant changes in the silica materials or in "MgSiO"-rich materials such as transient formation of Mg(OH)$_2$ that could be more common in primitive extraterrestrial materials than is currently appreciated. The most important findings of these hydration experiments are that hydrated amorphous magnesiosilica condensates may be quite common, and saponite proto-phyllosilicates could abound in icy-protoplanets. Sampling missions to comet nuclei, e.g., Stardust to comet Wild, should consider that there could be more water in the returned dust than current models predict but that these hydration experiments support.

that made it possible for us to improve our paper. The NASA Cosmochemistry Program supported the hydration experiments (J. Nuth). ATEM analyses were performed in the Electron Microbeam Analysis Facility of the Department of Earth and Planetary Sciences (University of New Mexico) where Fleur Rietmeijer-Engelsman provided technical support. The work was supported by NASA grants NAG5–11762 (Frans J. M. Rietmeijer) and NAG5–492 (R. N. Nelson) to Georgia Southern University.

Editorial Handling—Dr. Scott Sandford

REFERENCES

Alexander C. M. O'D, Barber D. J., and Hutchison R. 1989. The microstructure of Semarkona and Bishunpur. *Geochimica et Cosmochimica Acta* 53:3045–3057.

Bell J. F., Davis D. R., Hartmann W. K., and Gaffey M. J. 1989. Asteroids: The big picture. In *Asteroids II,* edited by Binzel R. P., Gehrels T., and Matthews M. S. Tucson: University of Arizona Press. pp. 921–945.

Bouwman J., Meeus G., de Koter A., Hony S., Dominik C., and Waters L. B. F. M. 2001. Processing of silicate dust grains in Herbig Ae/Be systems. *Astronomy and Astrophysics* 375:950–962.

Bradley J. P. 1988. Analysis of chondritic interplanetary dust thin-sections. *Geochimica et Cosmochimica Acta* 52:889–900.

Brearley A. J. 1993. Matrix and fine-grained rims in the unequilibrated CO3 chondrite ALH A77307: Origins and evidence for diverse, primitive nebular dust components. *Geochimica et Cosmochimica Acta* 57:1521–1550.

Brearley A. J. and Jones R. H. 1998. Chondritic meteorites. In *Planetary materials,* edited by Papike J. J. Washington D. C.: Mineralogical Society of America. pp. 1-398.

Brown P. G., Hildebrand A. R., Zolensky M. E., Grady M., Clayton R. N., Mayeda T. K., Tagliaferri E., Spalding R, MacRae N. D., Hoffman E. L., Mittlefehldt D. W., Wacker J. F., Bird J. A., Campbell M. D., Carpenter R., Gingerich H., Glatiotis M., Greiner E., Mazur M. J., McCausland P. J., Plotkin H., and Mazur T. R. 2000. The fall, recovery, orbit, and composition of the Tagish Lake meteorite: A new type of carbonaceous chondrite. *Science* 290:320–325.

Brownlee D. E. 1985. Cosmic dust: Collection and research. *Annual Review of Earth and Planetary Sciences* 13:147–173.

Bunch T. E. and Chang S. 1980. Carbonaceous chondrites—II. Carbonaceous chondrite phyllosilicates and light element geochemistry as indicators of parent body processes and surface conditions. *Geochimica et Cosmochimica Acta* 44:1543–1577.

Carrez P., Demyk K., Leroux H., Cordier P., Jones A. P., and d'Hendecourt L. 2002. Low-temperature crystallization of $MgSiO_3$ glasses under electron irradiation: Possible implications for silicate dust evolution in circumstellar environments. *Meteoritics & Planetary Science* 37:1615–1622.

Doremus R. H. 1995. Diffusion of water in silica glass. *Journal of Materials Research* 10:2379–2389.

Doremus R. H. and Perera G. 1991. Disssolution rates of silicate glasses in water at pH 7. *Journal of the American Ceramic Society* 74:1269–1274.

Emerich C., Lamarre J. M., Moroz V. I., Combes M., Sanko N. F., Nikolsky Y. V., Rocard F., Gispert R., Coron N., Bibring J. P., Encrenaz T., and Crovisier J. 1986. Temperature and size of the nucleus of Halley's comet deduced from I.K.S. infrared Vega 1 measurements. Proceedings, 20th ESLAB Symposium on the Exploration of Halley's Comet. European Space Agency SP-250, vol. 2. pp. 381–384.

Fabian D., Jäger C., Henning T., Dorschner J., and Mutschke H. 2000. Steps toward interstellar silicate mineralogy. V. Thermal evolution of amorphous magnesium silicates and silica. *Astronomy and Astrophysics* 364:282–292.

Fegley B., Jr. 1988. Cosmochemical trends of volatile elements in the solar system. In *Workshop on the origins of solar systems,* edited by Nuth J. A. and Sylvester P. LPI Technical Report 88-04. Houston: Lunar and Planetary Institute. pp. 51–60.

Fomenkova M. N., Kerridge J. F., Marti K., and McFadden L. A. 1992. Compositional trends in rock-forming elements of comet Halley dust. *Science* 258:266–269.

Grossman L. and Larimer J. W. 1974. Early chemical history of the solar system. *Reviews of Geophysics and Space Physics* 1:71–101.

Hallenbeck S. L., Nuth J. A., III, and Daukantes P. L. 1998. Mid-infrared spectral evolution of amorphous magnesium silicate smokes annealed in vacuum: Comparison to cometary spectra. *Icarus* 131:198–209.

Hartmann W. K., Tholen D. J., and Cruikshank D. P. 1987. The relationship of active comets, "extinct" comets, and dark asteroids. *Icarus* 69:33–50.

Hill H. G. M., Grady C. A., Nuth J. A., III, Hallenbeck S. L., and Sitko M. L. 2001. Constraints in nebular dynamics and chemistry based on observations of annealed magnesium silicate grains in comets and in disks surrounding Herbig Ae/Be stars. *Proceedings of the National Academy of Sciences* 98:2182–2187.

Jäger C, Henning T., Schlögl R., and Spillecke O. 1999. Spectral properties of carbon black. *Journal of Non-Crystalline Solids* 258:161–179.

Jenniskens P., Rietmeijer F. J. M., Brosch N., and Fonda M., editors. 2000. *Leonid storm research,* Dordrecht: Kluwer Academic Publishers. 606 p.

Jessberger E. K., Christoforidis A., and Kissel J. 1988. Aspects of major element composition of Halley's dust. *Nature* 332:691–695.

Kömle N. I. and Steiner G. 1992. Temperature evolution of porous ice samples covered by a dust mantle. *Icarus* 96:204–212.

MacKenzie K. J. D. and Meinhold R. H 1994. Thermal reactions of chrysotile revisited: A ^{29}Si and ^{25}Mg MAS NMR study. *American Mineralogist* 79:43–50.

Mackinnon I. D. R. and Kaser S. A. 1988. The clay-size fraction of CI chondrites Alais and Orgeuil: An AEM study (abstract). 19th Lunar and Planetary Science Conference. pp. 709–710.

Mackinnon I. D. R. and Rietmeijer F. J. M. 1987. Mineralogy of chondritic interplanetary dust particles. *Reviews of Geophysics* 25:1527–1553.

Martin B. and Fyfe W. S. 1970. Some experimental and theoretical observations on the kinetics of hydration reactions with particular reference to serpentinization. *Chemical Geology* 6:185–202.

Molster F. J., Waters L. B. F. M., and Tielens A. G. G. M. 2002. Crystalline silicate dust around evolved stars. II. The crystalline silicate complexes. *Astronomy and Astrophysics* 382:222–240.

Nelson R., Nuth J. A., and Donn B. 1987. A kinetic study of the hydrous alteration of amorphous MgSiO smokes: Implications for cometary particles and chondrite matrix. Proceedings, 17th Lunar and Planetary Science Conference. *Journal of Geophysical Research* 92:E657–R662.

Nelson R., Thiemens M., Nuth J., and Donn B. 1989. Oxygen isotopic fractionation in the condensation of refractory smokes. *Proceedings of the 19th Lunar and Planetary Science Conference,* edited by Ryder G. and Sharpton V. L. New York: Cambridge University Press and Lunar and Planetary Institute. pp. 559–563.

Newman A. C. D. 1987. The interaction of water with clay mineral

surfaces. In *Chemistry of clays and clay minerals,* edited by Newman A. C. D. Mineralogical Society Monograph 6. Essex: Longman Scientific & Technical. pp.237–274.

Nuth J. A. and Donn B. 1983. Laboratory studies of the condensation and properties of amorphous silicate smokes. Proceedings, 13th Lunar and Planetary Science Conference. *Journal of Geophysical Research* 88:A847–A852.

Nuth J. A., III and Hecht J. H. 1990. Signatures of aging silicate dust. *Astrophysics and Space Science* 163:79–94

Nuth J. A., III, Hallenbeck S. L., and Rietmeijer F. J. M. 1998. Interstellar and interplanetary grains, recent developments and new opportunities for experimental chemistry. *Earth, Moon, Planets* 80:73–112.

Nuth J. A., III, Hallenbeck S. L., and Rietmeijer F. J. M. 2000. Laboratory studies of silicate smokes: Analog studies of circumstellar materials. *Journal of Geophysical Research* 105: 10387–10396.

Nuth J. A., III, Rietmeijer F. J. M., and Hill H. G. M. 2002. Condensation processes in astrophysical environments: The composition and structure of cometary grains. *Meteoritics & Planetary Science* 37:1579–1590.

Nuth J. A., III, Donn B., Deseife R., Donn A., and Nelson R. 1986. Hydrous alteration of amorphous silicate smokes: First results. Proceedings, 16th Lunar and Planetary Science Conference. *Journal of Geophysical Research* 91:D533–D537.

Putnis A. and McConnell J. D. C. 1980. *Principles of mineral behavior.* Oxford: Blackwell Scientific Publications. 257 p.

Rietmeijer F. J. M. 1985. A model for diagenesis in proto-planetary bodies. *Nature* 313:293–294.

Rietmeijer F. J. M. 1992. A detailed petrological analysis of hydrated, low-nickel, nonchondritic stratospheric dust particles. Proceedings, 22nd Lunar and Planetary Science Conference. pp. 195–201.

Rietmeijer F. J. M. 1995. An analytical electron microscope (AEM) study of hydrous alteration of amorphous magnesiosilica smokes (abstract). 26th Lunar and Planetary Science Conference. pp. 1163–1164.

Rietmeijer F. J. M. 1996. An analytical electron microscope (AEM) study of hydrous alteration in a smoke of modal forsterite composition (abstract). 27th Lunar and Planetary Science Conference. pp. 1069–1070.

Rietmeijer F. J. M. 1998. Interplanetary dust particles. In *Planetary materials,* edited by Papike J. J. Washington D.C.: Mineralogical Society of America. pp. 1-95.

Rietmeijer F. J. M. 2002a. The earliest chemical dust evolution in the solar nebula. *Chemie der Erde* 62:1–45.

Rietmeijer F. J. M. 2002b. And just when you thought that the Leonid meteor storm held no more surprises: The 2001 storm (editorial). *Meteoritics & Planetary Science* 37:899–900.

Rietmeijer F. J. M. and Karner J. M. 1999. Metastable eutectics in the Al_2O_3-SiO_2 system explored by vapor phase condensation. *Journal of Chemical Physics* 110:4554–4558.

Rietmeijer F. J. M. and Nuth J. A., III. 2000a. Metastable eutectic equilibrium brought down to Earth. *EOS Transactions* 81:409, 414–415.

Rietmeijer F. J. M. and Nuth J. A., III. 2000b. Collected extraterrestrial materials: Constraints on meteor and fireball compositions. *Earth, Moon, Planets* 82/83:325–350.

Rietmeijer F. J. M. and Nuth J. A., III. 2001. Serpentine by hydrogenation of Fe-rich ferromagnesiosilica PCs in aggregate IDPs (abstract #1219). 32nd Lunar and Planetary Science Conference. CD-ROM

Rietmeijer F. J. M., Nuth J. A., III, and Mackinnon I. D. R. 1986. Analytical electron microscopy of Mg-SiO smokes: Comparison with XRD and Infrared studies. *Icarus* 65:211–222.

Rietmeijer F. J. M., Nuth, J. A., III, and Karner J. M. 1999a. Metastable eutectic condensation in a Mg-Fe-SiO-H_2-O_2 vapor: Analogs to circumstellar dust. *The Astrophysical Journal* 527: 395–404.

Rietmeijer F. J. M., Nuth J. A., III, and Karner J. M. 1999b. Metastable eutectic gas to solid condensation in the FeO-Fe_2O_3-SiO_2 system. *Physical Chemistry Chemical Physics* 1:1511–1516.

Rietmeijer F. J. M., Mukhin L. M., Fomenkova M. N., and Evlanov E. N. 1989. Layer silicate chemistry in P/comet Halley from PUMA-2 data (abstract). 20th Lunar and Planetary Science Conference. pp. 904–905.

Rietmeijer F. J. M., Nuth J. A., III, Jablonska M., and Karner J. M. 2000. Metastable eutectic equilibrium in natural environments: Recent developments and research opportunities. *Trends in Geochemistry* 1:29–51.

Rietmeijer F. J. M., Hallenbeck S. L., Nuth J. A., III, and Karner J. M. 2002a. Amorphous magnesiosilicate smokes annealed in vacuum: The evolution of magnesium silicates in circumstellar and cometary dust. *Icarus* 156:269–286.

Rietmeijer F. J. M., Nuth J. A., III, Karner J. M., and Hallenbeck S. L. 2002b. Gas to solid condensation in a Mg-SiO-H_2-O_2 vapor: Metastable eutectics in the MgO-SiO_2 phase diagram. *Physical Chemistry Chemical Physics* 4:546–551.

Rietmeijer F. J. M., Rotundi A., and Heymann D. Forthcoming. C_{60} and giant fullerenes in soot condensed in vapors with variable C/H_2 ratio. *Fullerenes, Nanotubes, and Carbon Nanostructures.*

Rotundi A., Rietmeijer F. J. M., Colangeli L., Mennella V., Palumbo P., and Bussoletti E. 1998. Identification of carbon forms in soot materials of astrophysical interest. *Astronomy and Astrophysics* 329:1087–1096.

Rotundi A., Brucato J. R., Colangeli L., Ferrini G., Mennella V., Palomba P., and Palumbo E. 2002. Production, processing and characterization techniques for cosmic dust analogues. *Meteoritics & Planetary Science* 37:1623–1635.

Schramm L. S., Brownlee D. E., and Wheelock M. M. 1989. Major element composition of stratospheric micrometeorites. *Meteoritics* 24:99–112.

Tazaki K., Fyfe W. S., and van der Gaast S. J. 1989. Growth of clay minerals in natural and synthetic glasses. *Clays and Clay Minererals* 37:348–354.

Thompson S. P. and Tang C. C. 2001. Laboratory investigation of crystallisation in annealed amorphous $MgSiO_3$. *Astronomy and Astrophysics* 368:721–729.

Tonui E. K., Zolensky M. E., Lipschutz M. L., Wang M. S., and Nakamura T. 2003. Yamato 86029: Aqueously altered and thermally metamorphosed CI-like chondrite with unusual textures. *Meteoritics & Planetary Science* 38:269–292.

Wegner W. W. and Ernst W. G. 1983. Experimentally determined hydration and dehydration reaction rates in the system MgO-SiO_2-H_2O. *American Journal of Science* 283:151–180.

Zolensky M. and Barrett R. 1994. Compositional variations of olivines and pyroxenes in chondritic interplanetary dust particles. *Meteoritics* 29:616–620.

Zolensky M. E. and Lindstrom D. 1992. Mineralogy of 12 large "chondritic" interplanetary dust particles. Proceedings, 22nd Lunar and Planetary Science Conference. pp. 161–169.

Zolensky M. E. and McSween H. Y., Jr. 1988. Aqueous alteration. In *Meteorites and the early solar system,* edited by Kerridge J. F. and Matthews M. S. Tucson: University of Arizona Press. pp. 114–143.

Zolensky M., Barrett R., and Browning L. 1993. Mineralogy and compositions of matrix and chondrule rims in carbonaceous chondrites. *Geochimica et Cosmochimica Acta* 57:3123–3148.